DOI: 10.1002/((please add manuscript number))
Article type: Communication

Bioinspired Metal-Organic Frameworks in Mixed Matrix Membranes for Efficient Static/Dynamic Removal of Mercury from Water

Rosaria Bruno, Marta Mon, Paula Escamilla, Jesus Ferrando-Soria, Elisa Esposito, Alessio Fuoco, Marcello Monteleone, Johannes C. Jansen,* Rosangela Elliani, Antonio Tagarelli, Donatella Armentano,* Emilio Pardo**

R. Bruno, Dr. R. Elliani, Dr. A. Tagarelli, Dr. D. Armentano,
Dipartimento di Chimica e Tecnologie Chimiche, Università della Calabria, 87036, Rende, Italy
E-mail: donatella.armentano@unical.it
Dr. E. Esposito, Dr. A. Fuoco, Dr. M. Monteleone, Dr. Johannes Carolus Jansen
Institute on Membrane Technology, CNR-ITM, Via P. Bucci 17/C, 87036 Rende, Italy
E-mail: johannescarolus.jansen@cnr.it
Dr. Marta Mon, Paula Escamilla, Dr. J. Ferrando-Soria, Dr. E. Pardo
Departamento de Química Inorgánica, Instituto de Ciencia Molecular (ICMOL), Universidad de Valencia, 46980 Paterna, Valencia, Spain
E-mail: emilio.pardo@uv.es

Keywords: metal-organic frameworks, mixed matrix membranes, water remediation, mercury(II), capture device

Abstract: We present the mercury removal efficiency of a novel MOF derived from the amino acid *S*-methyl-*L*-cysteine and characterize the process by single crystal X-ray crystallography. We further present a feasibility study on the performance of this MOF –and also that of another MOF derived from the amino acid *L*-methionine– when used as the sorbent in mixed matrix membranes (MMMs). These MOF-based MMMs exhibit high efficiency and selectivity –in both static and dynamic regimes– in the removal of Hg^{2+} from aqueous environments, due to the high density of thioalkyl groups decorating MOF channels. Both MMMs are capable to reduce different concentration of the pollutant to acceptable limits for drinking water (< 2 ppb). In addition, a novel device, consisting of the recirculation and adsorption of contaminated solutions through the MOF-MMMs, has been designed and successfully explored in the selective capture of Hg^{2+}. Thus, filtration of Hg^{2+} solutions with multiple passes through the permeation cell shows a gradual decrease of the pollutant concentration. These results suggest

the implementation of MOF-based MMMs in water remediation, after further optimization of their morphology, sorption capacity and permeability, with a large potential benefit on natural aquatic ecosystems helping to reduce either contaminants from accidental unauthorized or deliberate metal industrial dumping and to ensure access for clean and potable freshwater.

Contamination of aquatic systems[1] constitutes one of the most serious environmental problems faced by our modern society.[2] In this context, the United Nations (UN) agenda 2030[3] for sustainable development has set access to safe drinking water as one of its main objectives. At present, about half of the world population lives in areas with severe water stress, and this is expected to worsen in the next decades due to the unrestrained consumerism of current society and the concomitant global warming. In particular, among the plethora of contaminants arising from human activities, heavy metals represent one of the most important environmental concerns,[4,5] as a result of their toxicity, high persistence in the environment, great mobility in water and high tendency to accumulate in living beings.[6] Therefore, the development of efficient methods for the selective removal of heavy metals from aquatic environments attracts great interest. In contrast to the current methods for eliminating the organic contaminants – mainly based on the degradation by advanced oxidation processes (AOPs)[7], and in minor degree on the adsorption in porous materials[8]– the removal of heavy metals requires their physical capture. Existing methods include precipitation, coagulation/flocculation, membrane technology, and the adsorption by porous materials.[9] However, such currently available technologies, working separately, exhibit various shortcomings in terms of their still low efficiency, selectivity and, especially, processability and recyclability.[10]

A relatively new class of porous materials, defined as metal-organic frameworks (MOFs),[11–14] has emerged as one of the most promising candidates to overcome the aforementioned shortcomings.[15] When properly chosen, water-stable MOFs offer tunable microporosity, and the possibility to tailor their channels with the appropriate functionalities to enhance affinity for

contaminants in a selective manner.[15–17] For example, numerous MOFs and MOF-based materials have been reported for the successful removal of heavy metals like lead (Pb),[18–23] or mercury (Hg).[23–34] However, they exhibit important disadvantages such as difficult handling or losses/leakages of fine powders,[35] that need to be improved for their exploitation in industrial processes. In this context, with the aim to overcome these issues and make a step forward on MOF-based technologies for water remediation, we propose the use of MOF-based mixed matrix membranes (MMMs) –composite materials made up of homogeneously dispersed MOF-fillers in a porous polymer film– for mercury removal from water. A number of membrane-based processes for mercury removal from aqueous waste streams has been proposed in the literature, based on micro-, ultra- and nano-filtration or reverse osmosis,[36] supported liquid membranes,[37–39] liquid membranes with crown ethers[40] or benzoylthiourea[41] carriers, or ion exchange membranes.[42] However, MOF-based MMMs have mainly focused on industrially-relevant gas separation applications,[43–49] and their application for water remediation has been barely explored.[50–52] This includes removal of organic dyes,[53] arsenate,[54], humic acid,[55] for antifouling properties,[56] or simply to increase flux while rejecting impurities.[57] To the best of our knowledge, no MOF-based MMMs have been reported for the removal of mercury species from water.

We anticipate that the incorporation of the suitable MOF in the appropriate polymeric matrix with a specifically designed morphology, should yield a MMM that combines the superior capture properties of the MOF with improved handling and applicability of a polymer film. The scope of this work is to demonstrate the feasibility to immobilize task-specific MOFs, with exceptionally high selectivity for mercury, inside a tailor-made highly porous membrane, in order to guarantee high-water fluxes, i.e. productivity, and an efficient separation process, i.e. purity of the final products (Figure 1).

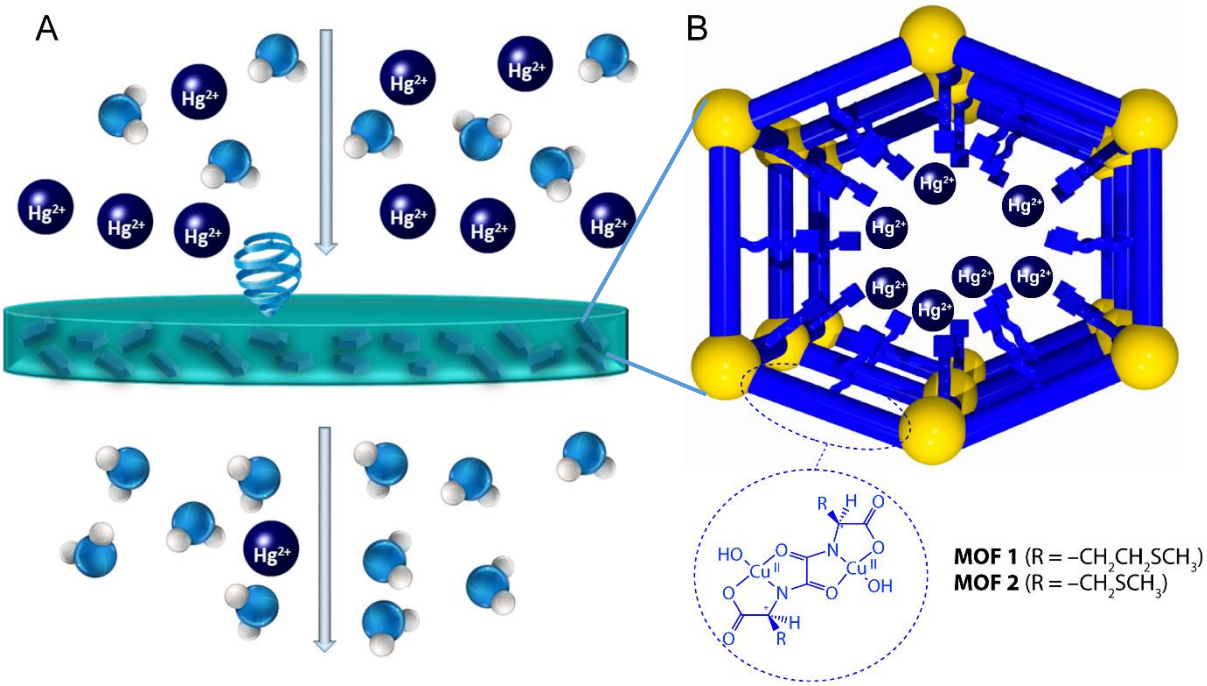

Figure 1. (A) Conceptualization of the filtration/adsorption process by means of a mixed matrix membrane in low pollutant concentration regimes. B) Detail of the interaction between contaminant and functional groups decorating MOFs channels.

In the search for highly performant materials for heavy metals removal, we have prepared two MMMs containing a previously reported MOF derived from the amino acid *L*-methionine[58] (Figure 2A) with formula $\{Ca^{II}Cu^{II}_6[(S,S)\text{-methox}]_3(OH)_2(H_2O)\}\cdot 16H_2O$ (**1**), and a novel MOF derived from the amino acid *S*-methyl-*L*-cysteine with formula $\{Ca^{II}Cu^{II}_6[(S,S)\text{-Mecysmox}]_3(OH)_2(H_2O)\}\cdot 16H_2O$ (**2**) (Figure 2B), where methox and Mecysmox ligands are bis[(*S*)-methionine]oxalyl diamide and bis[*S*-methylcysteine]oxalyl diamide, respectively. The high affinity of sulfur towards inorganic pollutants such as mercury is a well-known phenomenon, and makes these two MOFs promising candidates for the preparation of MMMs efficient for mercury removal from water.

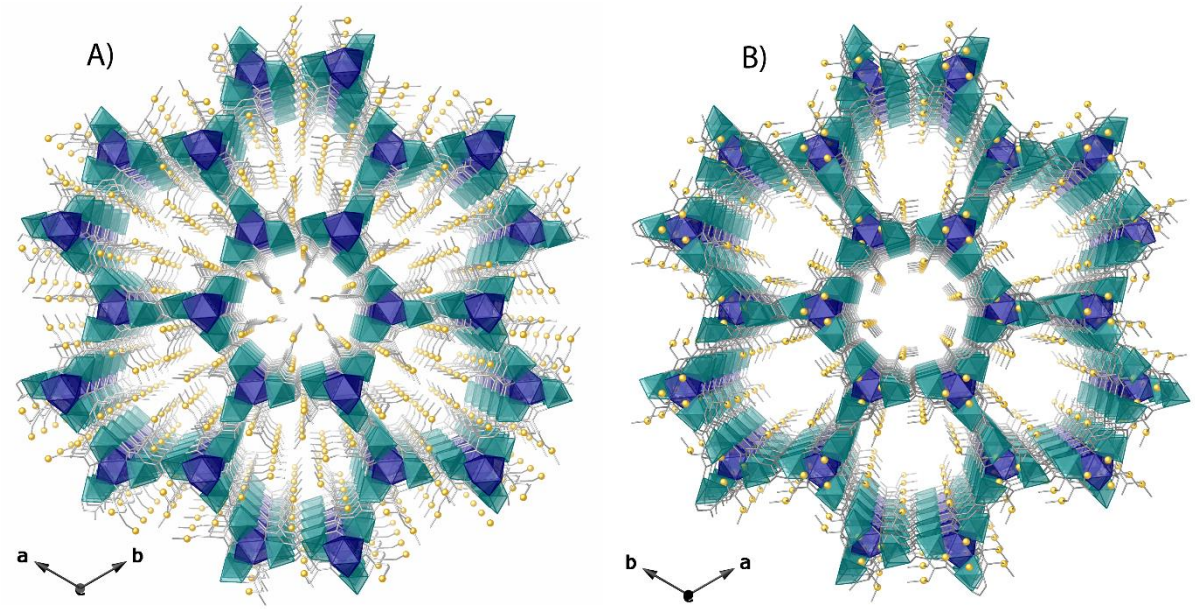

Figure 2. Perspective views along the direction of channel propagation for MOFs **1** (A) and **2 (**B) crystal structures.

Polycrystalline samples of **1** and **2** were obtained in multi-gram scale (see Experimental Section in Supporting Information) and characterized by ICP-MS, CHNS and TGA (Figure S1) analyses and PXRD measurements (Figure S2). Single crystals, suitable for X-ray diffraction, of **2** were also obtained by a slow diffusion method (see Experimental Section, Supporting Information) and its structure solved (*vide infra*) by Single-Crystal X-ray Diffraction (SCXRD) under synchrotron radiation. Both **1** and **2** were embedded in a porous polyimide matrix Matrimid®5218 by solution casting and nonsolvent-induced phase inversion, yielding two novel mixed matrix membranes named **1@Matrimid®** and **2@Matrimid®** (Figures 3 and S3).

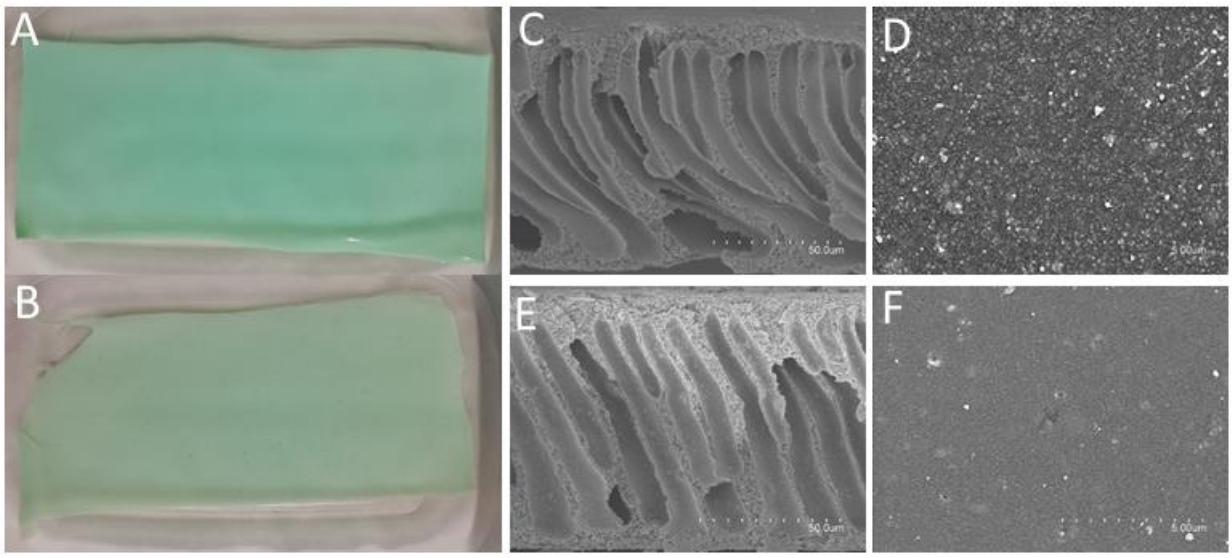

Figure 3. A,B) Optical Photograph of **1@Matrimid®** and **2@Matrimid®** after drying of the coagulated films show a very even distribution of the greenish MOFs. Cross-section C,E) and upper-layer D,F) SEM images of the membranes **1@Matrimid®** and **2@Matrimid®**, respectively.

For comparison with the MMMs, the efficiency of **1** and **2** in water remediation was first tested in their neat form. In this sense, the methionine-derived **1** had previously demonstrated very high Hg(II) removal efficiency in powder and pellet form.[25] In turn, the methylcysteine-derived MOF **2** is reported here for the first time. Thus, we evaluated the capture properties of **2** by soaking 10 mg of a polycrystalline sample of the MOF in an aqueous solution containing 10 ppm of the highly toxic Hg^{2+} cations and also other ions commonly present in drinking water, like Na^{+}, K^{+}, Ca^{2+}, Mg^{2+}, HCO_3^{-}, Cl^{-}, NO_3^{-} and SO_4^{2-}, in order to simulate real conditions. Quantification of the capture process *via* analysis of the ion concentration (Figure S4 and Table S1) as a function time for 72 h showed a very efficient and selective capture of Hg^{2+} by **2** under static conditions. In fact, **2** it is capable to reduce [Hg^{2+}] from 10 ppm to 4.6 ppb, close enough to acceptable limits for drinking water.[59] The capture process has much faster kinetics compared with the results reported previously for **1**,[25] which is in agreement with the higher accessible surface of **2** (see Figure 2B and structural description).

Taking advantage of the robustness and crystallinity of MOF **2** and aiming at unveiling the mechanisms governing its efficiency in Hg^{2+} capture, single-crystals of MOF **2** were soaked in a saturated $HgCl_2$ water/methanol solution for 48 h observing no degradation of the crystals. The crystal structure of the hybrid material $HgCl_2@\{Ca^{II}Cu^{II}_6[(S,S)\text{-mecysmox}]_3(OH)_2(H_2O)\}$ $8H_2O$ (**$HgCl_2$@2**) could be resolved by single crystal X-ray diffraction under synchrotron radiation. The structures of **2** and **$HgCl_2$@2**, are isoreticular to **1**,[58] crystallizing in the chiral $P6_3$ space group of the hexagonal system (Table S2). They consist of a uni-nodal **acs** chiral net built by calcium(II) vertexes and trans oxamidato-bridged dicopper(II) units, $\{Cu^{II}_2[(S,S)\text{-mecysmox}]\}$ (Figure 2B, 4, S5 S8), which act as linkers between the Ca^{II} ions through the carboxylate groups. In the resulting porous net, the functional flexible dimethyl thioether chains of the methylcysteine amino acid remain confined in hexagonal channels of *ca.* 0.3 nm (Figure B). The crystal structure of **$HgCl_2$@2** (Figure 4, S7 and S8) demonstrates that the $Cu^{II}Ca^{II}$ three-dimensional (3D) network of **2** (Figure 2B, S5 and S6) remains unaltered after the post-synthetic (PS) insertion process[60–62] (Table S2). The guest $HgCl_2$ molecules situate in the hexagonal channels of the MOF, being anchored to sulfur atoms from the dimethyl thioether groups decorating the walls of the pores (Figure 4). It confirms that the S···Hg interaction lies at the origin of the material receptor properties of **2** for the mercury capture process.

MOF **2** shows intrinsic flexibility, with one of the two crystallographically distinct dimethyl thioether chains exhibiting a distended conformation inward the pores. In this way, the MOF is able for grasping a fraction of the guest molecules, and forcing the other chain in an extremely bent conformation of the methyl groups to pinpoint a 50% of total Hg^{2+} ions in accessible interstitial sites, pointing along *c* axis (Figures 4C-D and S8). The Hg-S bond distances [2.225(3) and 2.23(4) Å] are in agreement with those found in the literature.[25,26]

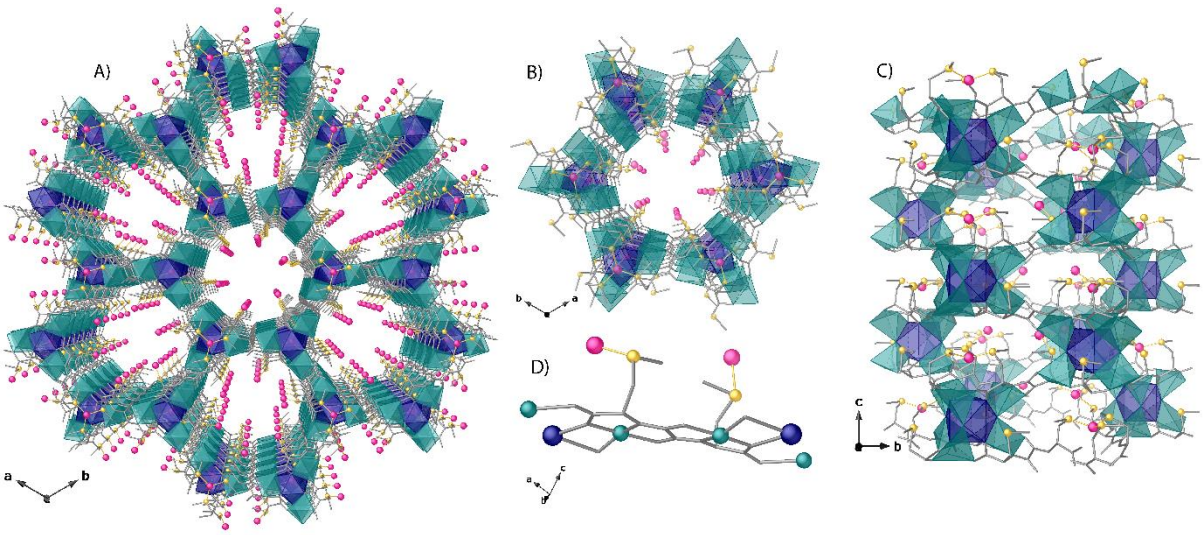

Figure 4. Crystal structure of adsorbate **$HgCl_2$@2**: A) Perspective views along the crystallographic *c* axis of the **$HgCl_2$@2** structure; B) Details of a single channel along c and C) a crystallographic axis: D) Highlight of the Hg···S coordinative interaction of the captured mercury species. Polyhedra: copper-cyan; calcium-blue. Spheres: mercury-purple; chlorine-green; sulfur-yellow; carbon from methyl groups-grey. Sticks: carbon, nitrogen and oxygen atoms from the ligand. Free water solvent molecules are omitted for clarity.

The formula of the adsorbate **$HgCl_2$@2** as $(HgCl_2)\{Ca^{II}Cu^{II}_6[(S,S)\text{-methox}]_3(OH)_2(H_2O)\} \cdot 8H_2O$ were further confirmed by ICP-MS, CHNS and TGA analyses (Figures S1 and Experimental Section in the Supporting Information).

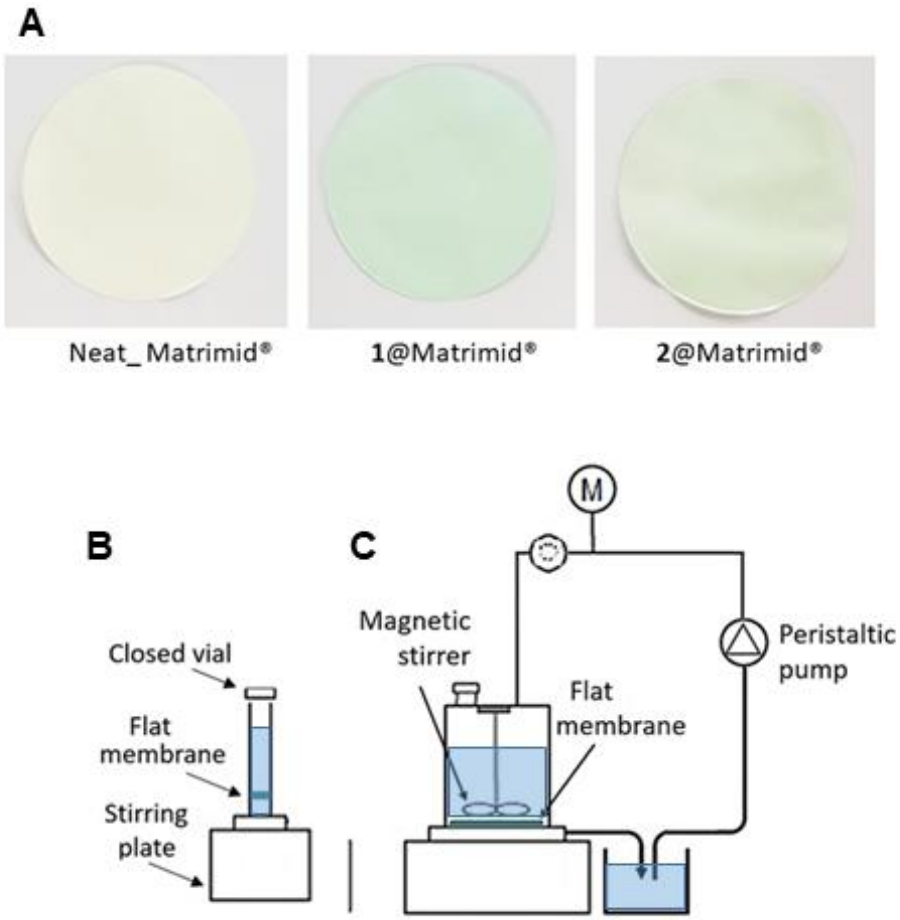

Figure 5. A) Photos of the circular samples of the three types of membranes tested with a diameter of 4.7 cm. Scheme of the static adsorption set-up B) and dynamic adsorption process C).

Based on the removal efficiency of **1** and **2**, both were embedded in mixed matrix membranes using Matrimid®5218 as polymer matrix, i.e. **1@Matrimid®** and **2@Matrimid®** with a loading of 30 wt%. 300 mg of polycrystalline samples of both MOFs were firstly activated at 80 °C under vacuum for 5 hours, and then homogeneously suspended in DMA (dimethylacetamide) using ultrasounds (30 minutes). Then, a solution containing 1 g of Matrimid® (20 wt% in DMA) was added to each MOF-suspension to form the casting solutions stirred for 24h. The membranes were prepared via non-solvent induced phase inversion (NIPS) by casting the solutions (using an Elcometer®3570 casting knife; casting gap = 250 µm) on a glass plate, and exposing for a 1 minute to room condition (relative humidity 35%) before their immersion into

the coagulation bath of distilled water. The membranes were washed with distilled water to remove traces of residual solvent, thoroughly dried and, finally, coated with a Hyflon® AD60x protective layer. The detailed procedure is given in the supporting information.

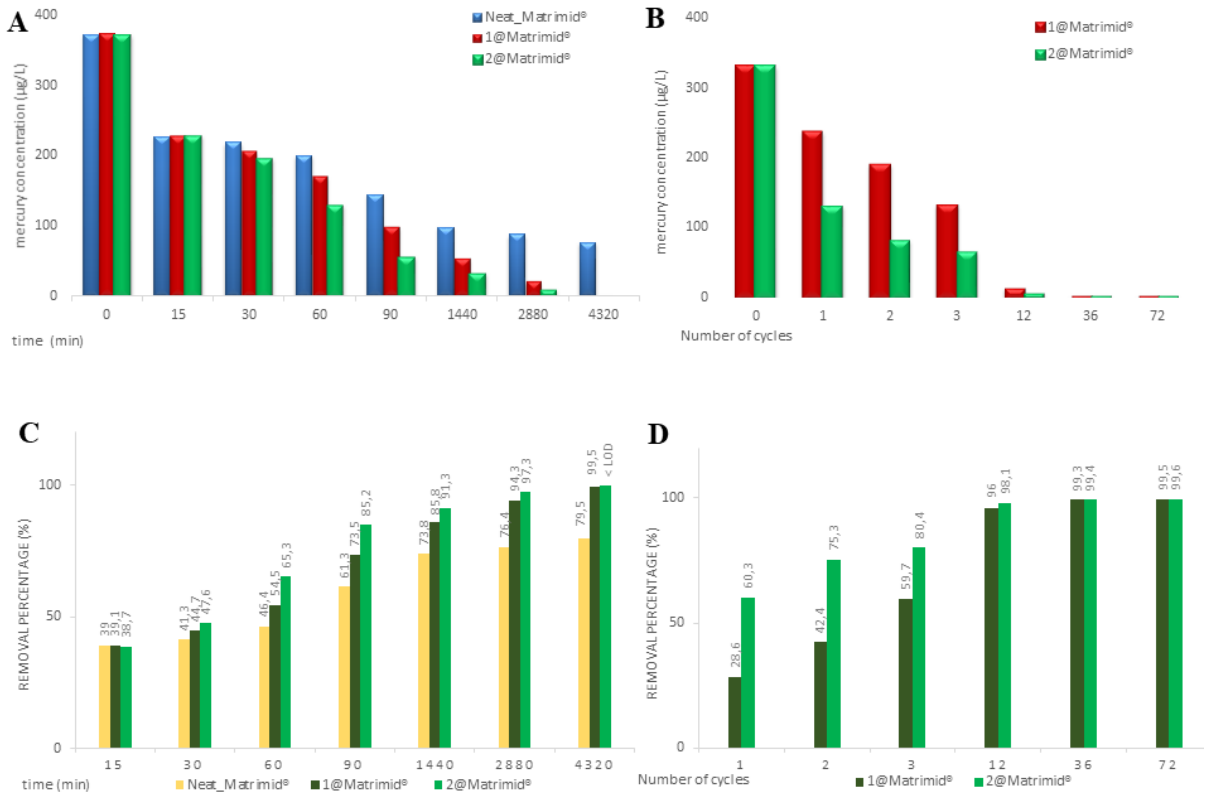

Figure 6. Kinetic profiles of the mercury (II) capture by **1@Matrimid®**, **2@Matrimid®** and neat **Matrimid®** membranes during soaking the corresponding circular flat membrane (surfaces of 17.34 cm^2) in aqueous solutions (oligo mineral water) of $HgCl_2$ in the 0-72 h interval. The initial [Hg^{2+}] in oligo mineral water are 370 ppb and 330 ppb for static adsorption (A) and microfiltration (dynamic) (B), respectively (Table S7). Removal efficiencies (%) of **1@Matrimid®**, **2@Matrimid®** and a pure **Matrimid®** membrane under the same conditions for static adsorption (C) and dynamic adsorption (D), respectively (Table S8). (Test with Neat Matrimid® in dynamic mode was not performed due to the low permeability of membrane and thus low flow, see Table S9. To ensure that the setup does not absorb mercury, an Hg^{2+} solution of 2.75 ppm was recirculated through the cell used in the dynamic adsorption experiment for 80 minutes. Through ICP-MS analysis, it was verified that there was no drop in concentration at the end of this procedure. Furthermore, each time a separate test with ICP-MS measuring [Hg^{2+}] of as-prepared solutions before and after recirculating has been performed to confirm that the Hg^{2+} is not considerably absorbed by the tubes, pump or other parts of the setup).

The loading of the MOFs is already visible to the unaided eye since it changes the membranes colors, which are yellowish for the neat Matrimid® membranes and green for the MMMs (Figure 5A). The TGA curves demonstrate that the MOFs in both MMMs do not significantly influence the pattern of the Matrimid® decomposition and they vary only slightly (Figure S9), most-likely due to the water contents of the MOF, which is reflected in a 5% weight loss in the temperature range of 50-400 °C for **1@Matrimid®** and **2@Matrimid®**. Above 600 °C, there is *ca.* 40% weight loss for **1@Matrimid®**, **2@Matrimid®** and the pure **Matrimid®** membrane, which must be due to the partial decomposition of Matrimid® (Figure S9, Supporting Information).

The MMMs **1@Matrimid®** and **2@Matrimid®** both have an asymmetric morphology with large finger-like voids in the center of the membrane and sponge-like layers near the top and bottom surface (Figure 3 and S3), while the neat Matrimid® membrane has a fully sponge-like structure (Figure S3). The very fine pore structure in the surface skin layer guarantees the efficient entrapment of the MOFs inside the membrane and reduces the chances of leaching. The latter is further improved by the impregnation with dilute Hyflon® AD solution.

The morphological structure of both membranes is characterized by the presence of a sponge-like layer in the top, which is thicker for **2@Matrimid®** (Figure 3E) compared to the **1@Matrimid®** (Figure 3F)**.** While both membranes exhibit a region with finger-like macrovoids under the top layer, due to the high demixing rate during membrane formation via NIPS, the morphology is suitable for microfiltration. It should be noted that optimum performance of the MMMs would require a completely sponge-like morphology, such as that of the neat Matrimid® membrane (Figure S3) (to guarantee a tortuous flow path and intense contact of the fluid with the MOFs), with a high overall porosity (to allow a high MOF loading) and small surface pores (to prevent MOF leakage) and high surface porosity (to guarantee high permeability). This may be achieved by careful optimization of numerous experimental parameters in the preparation method (type and concentration of polymer, type of solvent,

additives in the solvent, type of nonsolvent coagulation bath, solution temperature, casting temperature, coagulation temperature, additives in the coagulation bath, relative humidity, MOF size etc). However, even if the present membranes **1@Matrimid®** and **2@Matrimid®** have less effective large elongated voids, they are suitable for a convincing proof-of-principle. The membranes present a density of 0.33 g cm^{-3} and 0.34 g cm^{-3} for **1@Matrimid®** and **2@Matrimid®**, respectively, and both have a similar porosity of about 75%. Both membranes are stable in water and no MOF leaching is detected after the coating with Hyflon® AD60x, even after long storage of the produced membranes in water.

The Hg^{2+} removal efficiency of the two MMMs was studied by both static adsorption in batch (Figure 5B) and dynamic adsorption during permeation, adapting a microfiltration test cell (Figure 5C, 2.5 mL min^{-1}, feed pressure = 3 bar; see Table S3 and Figure S10), thus recirculating the contaminated solutions through the MOF-MMMs *via* a peristaltic pump. In both methods, three different solutions were used: deionized water with a high [Hg^{2+}] for benchmark experiments (Table S4), and oligo mineral water (see composition in Table S5) with two different [Hg^{2+}] in order to analyze the effect of other ions in solution in a more realistic situation (Tables S6-S7). The variation of the [Hg^{2+}] was monitored through ICP-MS analysis, which allowed to follow the absorption in a dynamic process.

In the experiments under static conditions with deionized water, the starting mercury concentration ([Hg^{2+}] = 2.61 ppm) dropped to 63 and 52 ppb after 48h, and even at 52.8 and 47.5 ppb after 72h with **1@Matrimid®** and **2@Matrimid®**, respectively (Figure S11A left and Table S3), which are values about seven times lower than the concentration reached by the neat Matrimid® membrane (348 ppb). Thus, the presence of both MOFs within the corresponding MMMs significantly increase the removal efficiency of the pure polymer, which was 98.0% for **1@Matrimid®** and 98.2 % for **2@Matrimid®** (Figure S11C left and Table S8). Under dynamic experiments by deionized water ([Hg^{2+}] = 2.21 ppm), the final concentrations after 48h were

302 and 275 ppb for **1@Matrimid®** and **2@Matrimid®**, respectively (Figure S11B right and Table S4). Thus, the removal efficiency for **1@Matrimid®** and **2@Matrimid®** are 82.8% and 89.2 %, respectively, demonstrating the suitability of these membranes for Hg^{2+} removal from water (Figure S11D right and Table S8). Static experiments using a solution of [Hg^{2+}] = 50 ppm showed that **1@Matrimid®** and **2@Matrimid®** exhibit maximum adsorption capacities of 540 and 690 mg g^{-1}, respectively, most-likely due to the higher surface area shown by **2** and suggesting higher efficiency for the removal of the target Hg^{2+}. Despite the maximum Hg^{2+} adsorption capacity of these novel MMMs are lower than the reported state-of-the-art thiol-functionalized COFs[63,64] or other MOFs composites,[23] they are largely enough to prove the validity of our approach; where carefully designed thioalkyl-based MOFs, derived from amino acids with high selectivity –at ppb levels– towards Hg^{2+}, are structured and implemented in MMMs without depletion of their activity and with the associated benefits toward real-world applications of membranes.

The presence of other ions in oligo mineral water slightly reduces the ability of **1@Matrimid®** to capture Hg^{2+}, whereas **2@Matrimid®** retains its performance, thus showing a higher selectivity for Hg^{2+} (Table S6 and Figure S12). Most likely the pore's dimension is at the origin of this behavior. Thus, despite the chemical similarity of the binding site, ensuring strong S···Hg interactions in **1** as in **2,** the longer aliphatic chain in **1**, reduces the size of the virtual diameter in **1** with respect to **2** (see X-ray structures).

At low [Hg^{2+}] in oligo mineral water, the Hg^{2+} concentration dropped from 370 ppb to 1.85 ppb after adsorption by **1@Matrimid®**, and below the 1.2 ppb detection limit for **2@Matrimid®** after 72 h under static conditions (Figure 6A and Table S7). Under dynamic conditions (Figure 6B and Table S7), the Hg^{2+} concentration decreased from the initial 330 ppb to 1.78 ppb with **1@Matrimid®** and to 1.26 ppb with **2@Matrimid®** after 48 h. These results reveal that both **1@Matrimid®** and **2@Matrimid®** are capable to remove Hg^{2+} from water (Figure 6C-D).

2@Matrimid® is able to capture up to the 99.9% of the Hg^{2+} cations from a realistic model solution (Figure 6D and Table S8), achieving values below the limits for drinking water established by the WHO[59] or the U.S. Environmental Protection Agency (EPA, < 2ppb for Hg^{2+}).[65]

For instance, a 30%wt MOF2/Matrimid® (**2@matrimid®**) membrane can purify 100mL of water from a dangerous 330 ppb level of [Hg^{2+}] to drinking water (1.26 ppb < 2 ppb EPA) by recirculating through the same membrane for two days (see also Table S9 for adsorption measured in 100 mL and expressed as μg/cm^2).

Capture experiments described above, demonstrate that the MOFs within the MMMs drastically improve the removal efficiency of the pure matrimid® polymer. Scanning Electron Microscopy coupled with Energy Dispersive X–ray (SEM/EDX) measurements of **1@Matrimid®** and **2@Matrimid®** loaded with $HgCl_2$ show the fundamental role of the MOFs in the Hg adsorption (Figures S13 and S14). EDX elemental mappings for Cu, Ca, S and Hg elements show a heterogeneous spatial distribution of Hg atoms through **1@Matrimid®** and **2@Matrimid®** with Hg atoms always located next to Cu, Ca and S atoms, which are part of the MOF particles. This confirms the prominent role of the MOF in the capture properties of the MOF-MMMs and suggesting that mercury atoms are bound by the thioether groups, as expected. Furthermore, while neat Matrimid does have a certain affinity for Hg (Figure 6a), in the presence of the MOFs, the Hg concentration in the polymer drops to very lower values, confirming not only the sorption capacity of the MOFs, but also their much higher affinity compared to that of the polymer matrix.

The stability of the membranes for a potential regeneration process was also evaluated. In this regard, Hg^{2+} was extracted after suspension of the membranes in a 10% (v/v%) aqueous solution of 2-mercaptoethanol for 24 hours. The integrity and reusability of **1@Matrimid®** and **2@Matrimid®** after the extraction process was studied over three subsequent cycles of adsorption and regeneration, which indicates the stability and still significant efficiency

(Supporting Information, Tables S10-S11 and Figures S15-S16) recovering up to 87.7 and 89.1% of Hg^{2+} of the original adsorption capacities for **1@Matrimid®** and **2@Matrimid,** respectively. The reusability of **1@Matrimid®** and **2@Matrimid®** should be also improved after optimization of the membrane morphology. Membranes stability and regeneration are key-factors for their exploitation in industrial applications since they have a direct impact on the economic feasibility.

In summary, the potential of MOFs and MOF-containing MMMs in water remediation, receives a very important boost with the reported results. Herein, in a first part, we have described the preparation and thorough physical characterization by means of synchrotron single-crystal X-ray crystallography of a novel MOF derived from amino acid *S*-methyl-*L*-cysteine (**2**) and the resulting adsorbate after mercury chloride removal (**$HgCl_2$@2**). Then, we showed two unprecedented MOF-MMMs –**1@Matrimid®** and **2@Matrimid®**, built up with Matrimid®5218 and two bioinspired MOFs highly performant in the capture of cationic Hg^{2+}– as a sustainable, effective and cheap solution for mercury removal from water, with the potential of minimizing the impact of this pollutant on the environment and human bodies. These features are due to the exquisite control of the thio-alkyl functionalities decorating the MOF pores that are used, to decontaminate, very efficiently –even from very low concentrations (ppb), which are usually found in real contaminated waters– aqueous environments to acceptable limits for potable water. Moreover, dynamic capture experiments have been also performed. Thus, a novel device –consisting of the recirculation and microfiltration of contaminated solutions through the MOF-MMMs *via* the use of a peristaltic pump– is reported here with outstanding capture results. These last results must be considered as a feasibility study for the proof-of-principle and open new avenues –after optimizing experimental conditions– for the use of MOF-MMMs in environmental remediation.

Experimental Section

See Supporting Information for a detailed description of MOFs and membranes preparation, their characterization and capture experiments.

[CCDC Deposition Numbers 2007971-2007972 contains the supplementary crystallographic data for this paper. These data can be obtained free of charge from The Cambridge Crystallographic Data Centre via www.ccdc.cam.ac.uk/data_request/cif.]

Supporting Information
Supporting Information is available from the Wiley Online Library or from the author.

Acknowledgements
((This work was supported by the Ministero dell'Istruzione, dell'Università e della Ricerca (Italy) and the Ministerio de Ciencia e Innovación (Spain) (Projects PID2019–104778GB–I00 and Excellence Unit "Maria de Maeztu" CEX2019-000919-M). R. B. thanks the MIUR (Project PON R&I FSE–FESR 2014–2020) for predoctoral grant. Thanks are also extended to the "2019 Post–doctoral Junior Leader–Retaining Fellowship, la Caixa Foundation (ID100010434 and fellowship code LCF/BQ/PR19/11700011" (J. F.–S.). M. M. thanks ITQ for the concession of a contract. D.A. acknowledges the financial support of the Fondazione CARIPLO / "Economia Circolare: ricerca per un futuro sostenibile" 2019, Project code: 2019–2090, MOCA. E.P. acknowledges the financial support of the European Research Council under the European Union's Horizon 2020 research and innovation programme / ERC Grant Agreement No 814804, MOF–reactors.))

References

[1] J. Murria, *Nat. Hazards Rev.* **2003**, *4*, 166.

[2] L. Xu, *Impact of Climate Change and Human Activity on the Eco-Environment*, Springer Berlin Heidelberg, Berlin, Heidelberg, **2015**.

[3] United Nations, "Transforming our world: the 2030 Agenda for Sustainable Development," **2015**.

[4] P. B. Tchounwou, C. G. Yedjou, A. K. Patlolla, D. J. Sutton, EXS, **2012**, pp. 133–164.

[5] S. N. Groudev, S. G. Bratcova, K. Komnitsas, *Miner. Eng.* **1999**, *12*, 261.

[6] H. Galal-Gorchev, *Food Addit. Contam.* **1993**, *10*, 115.

[7] D. B. Miklos, C. Remy, M. Jekel, K. G. Linden, J. E. Drewes, U. Hübner, *Water Res.* **2018**, *139*, 118.

[8] R. J. Drout, L. Robison, Z. Chen, T. Islamoglu, O. K. Farha, *Trends Chem.* **2019**, *1*, 304.

[9] S. Bhattacharya, A. B. Gupta, A. Gupta, A. Pandey, Eds. , *Water Remediation*, Springer Singapore, Singapore, **2018**.

[10] S. Bolisetty, M. Peydayesh, R. Mezzenga, *Chem. Soc. Rev.* **2019**, *48*, 463.

[11] H. Furukawa, K. E. Cordova, M. O'Keeffe, O. M. Yaghi, *Science* **2013**, *341*, 974.

[12] Y. Cui, B. Li, H. He, W. Zhou, B. Chen, G. Qian, *Acc. Chem. Res.* **2016**, *49*, 483.

[13] G. Maurin, C. Serre, A. Cooper, G. Férey, *Chem. Soc. Rev.* **2017**, *46*, 3104.

[14] A. Kirchon, L. Feng, H. F. Drake, E. A. Joseph, H.-C. Zhou, *Chem. Soc. Rev.* **2018**, *47*, 8611.

[15] S. K. Ghosh, Ed., *Metal-Organic Frameworks (MOFs) for Environmental Applications*, Elsevier, **2019**.

[16] M. Feng, P. Zhang, H.-C. Zhou, V. K. Sharma, *Chemosphere* **2018**, *209*, 783.

[17] J. Li, X. Wang, G. Zhao, C. Chen, Z. Chai, A. Alsaedi, T. Hayat, X. Wang, *Chem. Soc. Rev.* **2018**, *47*, 2322.

[18] R. Ricco, K. Konstas, M. J. Styles, J. J. Richardson, R. Babarao, K. Suzuki, P. Scopece, P. Falcaro, *J. Mater. Chem. A* **2015**, *3*, 19822.

[19] E. Tahmasebi, M. Y. Masoomi, Y. Yamini, A. Morsali, *Inorg. Chem.* **2015**, *54*, 425.

[20] H. Saleem, U. Rafique, R. P. Davies, *Microporous Mesoporous Mater.* **2016**, *221*, 238.

[21] L. Wang, X. Zhao, J. Zhang, Z. Xiong, *Environ. Sci. Pollut. Res.* **2017**, *24*, 14198.

[22] C. Yu, Z. Shao, H. Hou, *Chem. Sci.* **2017**, *8*, 7611.

[23] D. T. Sun, L. Peng, W. S. Reeder, S. M. Moosavi, D. Tiana, D. K. Britt, E. Oveisi, W. L. Queen, *ACS Cent. Sci.* **2018**, *4*, 349.

[24] Q.-R. Fang, D.-Q. Yuan, J. Sculley, J.-R. Li, Z.-B. Han, H.-C. Zhou, *Inorg. Chem.* **2010**, *49*, 11637.

[25] M. Mon, F. Lloret, J. Ferrando-Soria, C. Martí-Gastaldo, D. Armentano, E. Pardo, *Angew. Chem. Int. Ed.* **2016**, *55*, 11167.

[26] M. Mon, X. Qu, J. Ferrando-Soria, I. Pellicer-Carreño, A. Sepúlveda-Escribano, E. V. Ramos-Fernandez, J. C. Jansen, D. Armentano, E. Pardo, *J. Mater. Chem. A* **2017**, *5*, 20120.

[27] F. Ke, L.-G. Qiu, Y.-P. Yuan, F.-M. Peng, X. Jiang, A.-J. Xie, Y.-H. Shen, J.-F. Zhu, *J. Hazard. Mater.* **2011**, *196*, 36.

[28] J. He, K.-K. Yee, Z. Xu, M. Zeller, A. D. Hunter, S. S.-Y. Chui, C.-M. Che, *Chem. Mater.* **2011**, *23*, 2940.

[29] K.-K. Yee, N. Reimer, J. Liu, S.-Y. Cheng, S.-M. Yiu, J. Weber, N. Stock, Z. Xu, *J. Am. Chem. Soc.* **2013**, *135*, 7795.

[30] T. Liu, J.-X. Che, Y.-Z. Hu, X.-W. Dong, X.-Y. Liu, C.-M. Che, *Chem. Eur. J.* **2014**, *20*, 14090.

[31] F. Luo, J. L. Chen, L. L. Dang, W. N. Zhou, H. L. Lin, J. Q. Li, S. J. Liu, M. B. Luo, *J. Mater. Chem. A* **2015**, *3*, 9616.

[32] L. Liang, Q. Chen, F. Jiang, D. Yuan, J. Qian, G. Lv, H. Xue, L. Liu, H.-L. Jiang, M.

Hong, *J. Mater. Chem. A* **2016**, *4*, 15370.

[33] L. Huang, M. He, B. Chen, B. Hu, *J. Mater. Chem. A* **2016**, *4*, 5159.

[34] A. Chakraborty, S. Bhattacharyya, A. Hazra, A. C. Ghosh, T. K. Maji, *Chem. Commun.* **2016**, *52*, 2831.

[35] M. Mon, R. Bruno, J. Ferrando-Soria, D. Armentano, E. Pardo, *J. Mater. Chem. A* **2018**, *6*, 4912.

[36] M. Urgun-Demirtas, P. L. Benda, P. S. Gillenwater, M. C. Negri, H. Xiong, S. W. Snyder, *J. Hazard. Mater.* **2012**, *215–216*, 98.

[37] S. Weiss, V. Grigoriev, P. Mühl, *J. Memb. Sci.* **1982**, *12*, 119.

[38] S. Sangtumrong, P. Ramakul, C. Satayaprasert, U. Pancharoen, A. W. Lothongkum, *J. Ind. Eng. Chem.* **2007**, *13*, 751.

[39] K. Chakrabarty, P. Saha, A. K. Ghoshal, *J. Memb. Sci.* **2010**, *350*, 395.

[40] M. Shamsipur, M. H. Mashhadizadeh, G. Azimi, *Sep. Purif. Technol.* **2002**, *27*, 155.

[41] C. Fontàs, M. Hidalgo, V. Salvadó, E. Anticó, *Anal. Chim. Acta* **2005**, *547*, 255.

[42] A. Oehmen, D. Vergel, J. Fradinho, M. A. M. Reis, J. G. Crespo, S. Velizarov, *J. Hazard. Mater.* **2014**, *264*, 65.

[43] B. Seoane, J. Coronas, I. Gascon, M. E. Benavides, O. Karvan, J. Caro, F. Kapteijn, J. Gascon, *Chem. Soc. Rev.* **2015**, *44*, 2421.

[44] C. Y. Chuah, K. Goh, Y. Yang, H. Gong, W. Li, H. E. Karahan, M. D. Guiver, R. Wang, T. Bae, *Chem. Rev.* **2018**, *118*, 8655.

[45] Y. Liu, Z. Chen, G. Liu, Y. Belmabkhout, K. Adil, M. Eddaoudi, W. Koros, *Adv. Mater.* **2019**, *31*, 1807513.

[46] G. Liu, V. Chernikova, Y. Liu, K. Zhang, Y. Belmabkhout, O. Shekhah, C. Zhang, S. Yi, M. Eddaoudi, W. J. Koros, *Nat. Mater.* **2018**, *17*, 283.

[47] W. J. Koros, C. Zhang, *Nat. Mater.* **2017**, *16*, 289.

[48] B. Ghalei, K. Sakurai, Y. Kinoshita, K. Wakimoto, A. P. Isfahani, Q. Song, K.

Doitomi, S. Furukawa, H. Hirao, H. Kusuda, S. Kitagawa, E. Sivaniah, *Nat. Energy* **2017**, *2*, 17086.

[49] H. B. Park, J. Kamcev, L. M. Robeson, M. Elimelech, B. D. Freeman, *Science* **2017**, *356*, eaab0530.

[50] A. Elrasheedy, N. Nady, M. Bassyouni, A. El-Shazly, *Membranes (Basel).* **2019**, *9*, DOI 10.3390/membranes9070088.

[51] M. Kalaj, K. C. Bentz, S. Ayala, J. M. Palomba, K. S. Barcus, Y. Katayama, S. M. Cohen, *Chem. Rev.* **2020**, acs.chemrev.9b00575.

[52] B.-M. Jun, Y. A. J. Al-Hamadani, A. Son, C. Min Park, M. Jang, A. Jang, N. Chan Kim, Y. Yoon, *Sep. Purif. Technol.* **2020**, 116947.

[53] M. M. Baneshi, A. M. Ghaedi, A. Vafaei, D. Emadzadeh, W. J. Lau, H. Marioryad, A. Jamshidi, *Environ. Res.* **2020**, *183*, 109278.

[54] P. Wan, M. Yuan, X. Yu, Z. Zhang, B. Deng, *Chem. Eng. J.* **2020**, *382*, 122921.

[55] M. U. M. Junaidi, C. P. Leo, S. N. M. Kamal, A. L. Ahmad, *Water Sci. Technol.* **2013**, *67*, 2102.

[56] F. Mohammadnezhad, M. Feyzi, S. Zinadini, *J. Ind. Eng. Chem.* **2019**, *71*, 99.

[57] A. Karimi, A. Khataee, V. Vatanpour, M. Safarpour, *Sep. Purif. Technol.* **2019**, *229*, 115838.

[58] M. Mon, J. Ferrando-Soria, T. Grancha, F. R. Fortea-Pérez, J. Gascon, A. Leyva-Pérez, D. Armentano, E. Pardo, *J. Am. Chem. Soc.* **2016**, *138*, 7864.

[59] World Health Organisation, *Guidelines for Drinking-Water Quality, Fourth Edition*, **2011**.

[60] J. D. Evans, C. J. Sumby, C. J. Doonan, *Chem. Soc. Rev.* **2014**, *43*, 5933.

[61] S. M. Cohen, *J. Am. Chem. Soc.* **2017**, *139*, 2855.

[62] M. Mon, J. Ferrando-Soria, M. Verdaguer, C. Train, C. Paillard, B. Dkhil, C. Versace, R. Bruno, D. Armentano, E. Pardo, *J. Am. Chem. Soc.* **2017**, *139*, 8098.

[63] L. Merí-Bofí, S. Royuela, F. Zamora, M. L. Ruiz-González, J. L. Segura, R. Muñoz-Olivas, M. J. Mancheño, *J. Mater. Chem. A* 2017, **5**, 17973– 17981.

[64] Q. Sun, B. Aguila, J. Perman, N. Nguyen, S. Q. Ma, *J. Am. Chem. Soc.* 2016, **138**, 15790– 15796.

[65] U.S. Environmental Protection Agency, "2012 ed. of the Drinking Water Standards and Health Advisories," **2012**.

Supporting Information

Bioinspired Metal-Organic Frameworks in Mixed Matrix Membranes for Efficient Static/Dynamic Removal of Mercury from Water

Rosaria Bruno, Marta Mon, Paula Escamilla, Jesus Ferrando-Soria, Elisa Esposito, Alessio Fuoco, Marcello Monteleone, Johannes C. Jansen,* Rosangela Elliani, Antonio Tagarelli, Donatella Armentano,* Emilio Pardo**

Experimental Section

Preparations

Chemical: All chemicals were of reagent grade quality. They were purchased from commercial sources and used as received. The powder of polyimide (PI) Matrimid®5218 was degassed at 453 K overnight under vacuum to remove the adsorbed water. Compound **{$Cu_6Ca[(S,S)$-methox]$_3(OH)_2(H_2O)\} \cdot 16H_2O$ (1)** was prepared as reported earlier (Ref. 57 in the main text).

Preparation of HMeEt-(S,S)-Mecysmox [bis[(S)-methycysteine]oxalyl diamide]: The proligand was prepared using the following synthetic procedure: First, under a N_2 atmosphere, an excess of thionyl chloride (13.10 mL, 180 mmol) was added dropwise, under stirring at 0 °C on an ice-bath, to a solution of (*S*)-methyl-(*L*)-cysteine amino acid (8.11 g, 60 mmol) in 150 mL of MeOH. The resulting colorless solution was refluxed for 6 hours. Then, the excess of thionyl chloride was distilled with MeOH (3 x 150 mL). The reaction mixture was washed with acetone (150 mL) and diethyl ether (100 mL) and further concentrated, under reduced pressure, to afford the methyl ester derivative of the (*S*)-methyl-(*L*)-cysteine amino acid, which was used in the next step without further purification. Second, the resulting methyl ester derivative of the (*S*)-methyl-(*L*)-cysteine amino acid (8.95 g, 60 mmol) was dissolved in 250 mL of dichloromethane and charged with triethylamine (8.4 mL, 60 mmol). To the resulting colorless reaction mixture, was added dropwise another solution containing oxalyl chloride (2.54 mL, 30.0 mmol) in dichloromethane (150 mL) under vigorous stirring at 0 °C on an ice-bath. The resulting solution was further stirred during two hours. The small amount of white solid (Et_3NHCl) formed was filtered off and the resulting solution was then concentrated in a rotatory evaporator to a final volume of 100 mL. The pale-yellow solution was washed three times with water (3x50 mL) and finally, the solvent was removed in a rotatory evaporator to afford a white solid, which was collected with water and dried under vacuum. Yield: 9.62 g, 91%; Anal. calcd (%) for $C_{12}H_{20}S_2N_2O_6$ (352.4): C 40.98, H 5.72, S 18.20, N 7.95; found: C 40.97, H 5.68, S 18.26, N 7.99; ^{1}H NMR ([D_6]DMSO): 2.20 (s, 6H; SCH_3), 2.97 (m, 2H; CH_2), 3.17 (m, 2H; CH_2), 3.62 (s, 6H; OCH_3), 4.78 (t, 2H; CH), 9.01 (d, 2H; NH from CONH). IR (KBr): ν = 1763, 1751and 1656 cm^{-1} (C=O).

Preparation of $(Me_4N)_2\{Cu_2[(S,S)$-Mecysmox$](OH)_2\} \cdot 5H_2O$: An aqueous suspension (60 mL) of H_2Me_2-(S,S)-Mecysmox (10.572 g, 30 mmol) was treated with a 25% methanolic solution of Me_4NOH (36 mL, 125 mmol) until complete dissolution. Another aqueous solution (25 mL) of $CuCl_2$ (8.07 g, 60 mmol) was then added dropwise while the reaction mixture was stirred. The resulting deep green solution was concentrated to a volume of *ca.* 5-10 mL in a rotary

evaporator affording a green polycrystalline solid that was gently washed with acetone filtered off and dried under vacuum. Yield: 14.77 g, 68%; Anal.: calcd for $C_{18}H_{48}Cu_2S_2N_4O_{13}$ (719.8): C, 30.03; H, 6.72; S, 8.91; N, 7.78%. Found: C, 30.13; H, 6.63; S, 8.93; N, 7.75%. IR (KBr): ν = 3621 cm^{-1} (O-H), 3023, 2964 cm^{-1} (C-H), 1608 cm^{-1} (C=O).

*Preparation of $\{Ca^{II}Cu^{II}_6[(S,S)\text{-}Mecysmox]_3(OH)_2(H_2O)\} \cdot 16H_2O$ (**2**):* $(Me_4N)_2\{Cu_2[(S,S)\text{-}Mecysmox](OH)_2\} \cdot 4H_2O$ (4.32 g, 6.0 mmol) was dissolved in 50 mL of water. Then, another aqueous solution (10 mL) containing $CaCl_2$ (0.22 g, 2.0 mmol) was added dropwise under stirring. After further stirring for 10 h, at room temperature, a green polycrystalline powder was obtained and collected *via* filtration and dried with ethanol, acetone and diethyl ether. Yield: 2.91 g, 83%; Anal.: calcd for $C_{30}Cu_6CaH_{72}S_6N_6O_{37}$ (1722.7): C, 20.92; H, 4.21; S, 11.17; N, 4.88%. Found: C, 20.91; H, 4.17; S, 11.19; N, 4.93%. IR (KBr): ν = 1602 cm^{-1} (C=O). Well-shaped hexagonal prisms of **1** suitable for X-ray structural analysis could be obtained by slow diffusion, in an H-shaped tube, of H_2O/DMF (1:9) solutions containing stoichiometric amounts of $(Me_4N)_2\{Cu_2[(S,S)\text{-}Mecysmox](OH)_2\} \cdot 5H_2O$ (0.13 g, 0.18 mmol) in one arm and $CaCl_2$ (0.0067 g, 0.06 mmol) in the other. They were isolated by filtration on paper and air-dried.

*Preparation of $HgCl_2$@$\{Ca^{II}Cu^{II}_6[(S,S)\text{-}Mecysmox]_3(OH)_2(H_2O)\} \cdot 8H_2O$ (**$HgCl_2$@2**):* Well-formed hexagonal green prisms of **$HgCl_2$@2**, which were suitable for X-ray diffraction, were obtained by soaking crystals of **2** (5.0 mg) in saturated aqueous and H_2O/CH_3OH (1:1) solutions of $HgCl_2$ for 48 hours. The crystals were washed with water, isolated by filtration on paper and air-dried. **$HgCl_2$@2**: Anal.: calcd for $C_{30}Cl_2Cu_6CaH_{56}HgS_6N_6O_{29}$ (1850.0): C, 19.48; H, 3.05; S, 10.40; N, 4.54%. Found: C, 19.51; H, 3.09; S, 10.37; N, 4.51%. IR (KBr): ν = 1601 cm^{-1} (C=O).

Preparation of mixed matrix membranes: A homogeneous 20 wt% dope solution of Matrimid® was prepared by dissolving 6 g of powder polymer in 24 g of DMA under magnetic stirring at room temperature for 24 h. The powder of polycrystalline MOFs **1** and **2** were activated at 80 °C in an oven under vacuum for 5 hours, and then suspended in dimethylacetamide (DMA). Sonication for 30 minutes yielded homogenous suspensions of both MOFs to which 5 g of the polymer solution of Matrimid® 5218 was added. The resulting solution/suspension was stirred for 24 hours. Then the solution was cast on a glass plates by means of a casting knife (Elcometer®3570) with a gap of 250 μm, exposed to the air for 1 minute, and then immersed in the coagulation bath, consisting of distilled water, to form the final membranes by non-solvent induced phase separation (NIPS).
The obtained membrane was left in the coagulation bath for 72 hours, then washed in ethanol and left to dry in air in order to remove residual traces of solvent. The dry membrane was coated with a protective layer of Hyflon® AD60x by means of a dip-coating procedure using a solution of Hyflon® AD60x in HFE 7100 (hydrofluoroether) at 0.1 wt%. It is a crucial point the very low thickness of layer to avoid permeability decrease. Reference membrane of pure Matrimid®5218 was prepared by the same procedure.

Characterization
Physical Techniques: Elemental (C, H, N), SEM and ICP-MS analyses (of the pure MOFs **1** and **2**) and titration experiments were performed at the Microanalytical Service of the Universitat de València. ICP-MS analyses for the Hg^{2+} capture experiments on membranes (*vide infra*) were performed at the Department of Chemistry of the University of Calabria. FT–IR spectra were recorded on a Perkin-Elmer 882 spectrophotometer as KBr pellets. The thermogravimetric analysis was performed on crystalline samples under a dry N_2 atmosphere with a Mettler Toledo TGA/STDA 851^e thermobalance operating at a heating rate of 10 ºC min^{-1}.

X-ray Powder Diffraction Measurements: Polycrystalline samples of **2**, and **$HgCl_2$@2**, were introduced into 0.5 mm borosilicate capillaries prior to being mounted and aligned on a Empyrean PANalytical powder diffractometer, using Cu Kα radiation (λ = 1.54056 Å). For each sample, five repeated measurements were collected at room temperature (2θ = 2–60°) and merged in a single diffractogram.

X-ray crystallographic data collection and structure refinement: Crystals of **2** and **$HgCl_2$@2** were selected and mounted on a MITIGEN holder in Paratone oil and very quickly placed in a nitrogen stream cooled at 100 K to avoid the possible degradation upon desolvation or exposure to air. Diffraction data were collected using synchrotron radiation at I19 beamline of the Diamond Light Source at λ = 0.6889 Å and processed through *xia2* software.[1] The structures were solved with the SHELXS structure solution program, using the Patterson method. The model was refined with version 2018/3 of SHELXL against F^2 on all data by full-matrix least squares. [2]

Bearing in mind that, crystals of **$HgCl_2$@2**, suitable for X-ray diffraction, were obtained by soaking crystals of **2** in saturated aqueous and H_2O/CH_3OH (1:1) solutions of $HgCl_2$, thus after a crystal-to-crystal transformation, it is reasonable to observe a diffraction pattern sometimes affected by expected internal imperfections of the crystals that give a quite expected difficulty to perform a perfect correction of anisotropy (detected as Alerts A in the checkcifs). However, the solution and refinement parameters are pretty above of the standard MOFs structures generally reported.

In **$HgCl_2$@2 t**he occupancy factors, of $HgCl_2$ molecules have been defined in agreement with SEM results performed on loaded MOFs. The use of some C-C and C-S bond lengths restrains during the refinements or fixed positions of some highly disordered atoms, has been reasonable imposed and related to extraordinary flexibility of amino acid chains of the Mecysmox ligand that are dynamic components of the frameworks. In the refinement of both crystal structures some further restrains, to make the refinement more efficient, have been applied, for instance in **$HgCl_2$@2** ADP components have been restrained to be similar to other related atoms, using SIMU for disordered sections or EADP for group of atoms of amino acid chains and the guest molecules, in **$HgCl_2$@2,** expected to have essentially similar ADPs.

The solvent molecules were highly disordered as expected in porous crystals and for that reason have not been modeled, the quite large channels featured by this series of MOFs likely account for that. The hydrogen atoms of the ligand, except for the hydroxo/water oxygen atom O(1H) (where the OH/H_2O statistic distribution is 2:1) both in **2** and **$HgCl_2$@2** were set in calculated positions and refined as riding atoms. The contribution to the diffraction pattern from the highly disordered and undetected solvent molecules located in the voids was subtracted from the observed data through the SQUEEZE method, implemented in PLATON.[3]

[1] (a) Evans, P. Scaling and assessment of data quality. *Acta Cryst. D* **62**, 72–82 (2006). (b) Evans, P. R., Murshudov, G. N. How good are my data and what is the resolution? *Acta Cryst. D* **69**, 1204–1214 (2013). (c) Winn, M. D. *et al*. Overview of the *CCP4* suite and current developments. *Acta Cryst. D* **67**, 235–242 (2011). (d) Winter, G. *xia2*: and expert system for macromolecular crystallography data reduction. *J. Appl. Cryst.* **43**, 186–190 (2010). (e) Winter, G. *et al*. *DIALS*: implementation and evaluation of a new integration package *Acta Cryst*. **2018**, D74, 85-97.

[2] (a) Sheldrick, G. M. *Acta Cryst.* **A64**, 112-122 (2008). (b) Sheldrick, G. M. *Acta Cryst. Sect. A Found. Adv*. **71**, 3–8 (2015).

A summary of the crystallographic data and structure refinement for the three compounds is given in Table S2. The comments for the alerts A and B are described in the CIFs using the validation reply form (vrf). CCDC Deposition Numbers are 2007971-2007972 for **2** and **$HgCl_2$@2**, respectively.

The final geometrical calculations on free voids and the graphical manipulations were carried out with PLATON [3] implemented in WinGX, [4] and CRYSTAL MAKER [5] programs, respectively.

Membrane characterization: The surface and the cross-section morphology of the membranes were characterized by scanning electron microscopy with a HITACHI model S-4800 SEM. The samples for cross-section SEM characterization were prepared by freeze fracturing in liquid nitrogen, in order to avoid deformation of the sample during the fracturing procedure. SEM characterization was performed using the Ultra High-resolution Electron Beam Lithography and SEM imaging system with accelerating voltage of 5 kV. Only then Neat_Matrimid® sample was deposited an ultrathin gold layer using the sputter coater, model KW-4a, Chemat technology for 18 seconds and 500 rpm.

Samples were analyzed without and with a sputter-coating with gold. The images before and after the coating procedure are shown in Figure S3.

The MOF is homogenously distributed across the membrane. No particles sedimentation or agglomeration phenomena were observed. The cross section morphology of both membranes is characterized by the presence of a sponge-like layer in the top with an average thickness about 5 μm. This is the effective layer of the MMMs that promotes the actual contact between Hg^{2+} and sulfur-functional groups of MOF, during the water flow.

Thermogravimetric Analysis. The thermogravimetric analysis was performed on membrane samples under a dry N_2 atmosphere with a Mettler Toledo TGA/STDA 851^e thermobalance. The experiments were carried out within a temperature range from 25 °C up to 800 °C at a heating rate of 10 K/min. Approximately 20 mg of the membrane was placed in a ceramic pan for the measurements.

Permeability measurements of the membranes in distilled water and low mineral water. The study of water permeability transport properties was carried out by using a Millipore UF Solvent-resistant Stirred Cell 47 mm XFUF04701 cell. The membrane is located in a circular compartment with an area of 17 cm^2, but the effective membrane area that participated to the separation process is about 13.84 cm^2, because the membrane is held in plane and at the same time protected by an o-ring with a diameter of 4.2 cm. The flow filtration setup is illustrated in Figure 5. The water solution was fed to upper side of the membrane by means of a circulation pump and forced to flow through the membrane under a given trans-membrane pressure, which was set by regulating the recirculation speed of the solution until the desired pressure was reached. All experiments were carried out at 25 °C. The water flux (Jw) is determined from the volume of permeate (V_P) collected per unit of time (t) through the given membrane surface area (A) at fixed trans-membrane pressure (ΔP) values:

[3] (a) Spek, A. L. *Acta Crystal. Sect. D, Biol. Crystal.* **65**, 148 (2009). b) Spek, A. L. *Acta Crystal. Sect. C-Struct. Chem*. **71**, 9-18 (2015).
[4] Farrugia, L. J. *J. Appl. Crystallogr.* **1999**, *32*, 837.
[5] D. Palmer, CRYSTAL MAKER, Cambridge University Technical Services, C. No Title, 1996.

$$Jw = \frac{Vp}{t \times A}$$

The measurements of the permeation rate were performed at steady-state conditions under different ΔP. The water permeance is defined as:

$$Pw = \frac{Jw}{\Delta P}$$

and is obtained from the slope of the plot of *Jw vs. ΔP*

By using the cell, it was possible to apply a pressure gradient to a certain volume of distilled water that would pass through the membrane. In view of the experiment in the low mineral content matrix for greater accuracy of the data, the flow and permeance values (Table S3 and Figure S10) for each membrane were recorded, also in this other matrix, in this specific case commercial water was used (Table S5).

Hg^{2+} Capture experiments

Prior to the evaluation of the MMMs removal efficiency, the capture behavior of MOF **2** was first evaluated. 10 mg of a polycrystalline sample of **2** was soaked in an aqueous solution containing 10 ppm of Hg^{2+} cations and also other common ions found in drinking water like Na^+, K^+, Ca^{2+}, Mg^{2+}, HCO_3^-, Cl^-, NO_3^- and SO_4^{2-}. The capture process was monitored, through ICP-MS analyses and results are shown in Figure S5.

Thereafter, static and dynamic adsorption experiments were performed on circular sections of flat micro-porous membranes (**1@Matrimid®**, **2@Matrimid®** and pure Matrimid®) with an area of 13.84 cm^2 (Data reported on Tables S3-S7). First of all, the capture of mercury(II) in distilled water was verified. In addition, in order to mimic the real conditions of polluted matrices, two other experiments were conducted in an oligomineral matrix contaminated by different concentrations of mercury. The experiment with higher concentration (oligomineral matrix I) is aimed to demonstrate the efficiency of the device, while lowering the amount of contaminant (oligomineral matrix II), it has been shown that due to the strong affinity of MOFs for mercury, the device is not only effective but also sensitive towards the capture of small quantities (traces) of mercury(II).

During the dynamic adsorption, the mixed matrix membranes were placed in contact with a solution containing mercury chloride at a known concentration, recirculating 100 mL of volume in the Millipore UF Solvent-resistant Stirred Cell 47 mm cell XFUF04701. A Masterflex L / S Economy Variable-Speed Drive, 20 to 600 rpm, 115 VAC peristaltic pump was used for the recirculation of the solution.

The analysis on samples were performed for a total number of 72 cycles (a cycle to recirculate 100 mL of the mercury polluted solution; it is performed in 40 minutes). The stabilization of the mercury in view of the ICP-MS analysis occurred by adding nitric acid. After each cycle, a volume of 200 µl of solution was picked up and stabilized for ICP-MS analysis of mercury by addition of 200 µl of nitric acid with a purity of 98 %. The ICP-MS data are reported considering the dilution factor.

Firstly, the effective capture in distilled water was assessed, then, to confirm the effectiveness of the membranes in operating conditions close to the real matrices, commercial mineral water with a defined mineral composition was used (reported in Table S5).
In the case of static adsorption, the three different types of membrane were placed in contact with 100 mL of a solution with a known concentration of mercury(II) chloride. Data reported in Tables S4, S6-S7. The stabilization of the mercury in solution, in view of the ICP-MS analyses, was carried out by adding concentrated nitric acid.

Microscopy measurements

Scanning Electron Microscopy (SEM) Imaging of the membrane surface and cross sections (**1@Matrimid®** and **2@Matrimid®** and pure **Matrimid®**) was carried out on a LEO 420 SEM. Samples were freeze-fractured in liquid nitrogen and were not sputter coated with gold before analysis.

Scanning Electron Microscopy (SEM) elemental analysis was carried out for **1@Matrimid®** and **2@Matrimid®** after Hg adsorption, using a HITACHI S-4800 electron microscope coupled with an Energy Dispersive X–ray (EDX) detector. Data was analyzed with QUANTAX 400. Both membranes were suspended in a 100 ppm $HgCl_2$ aqueous solution for 24 h. and then introduced in pure water for 15 minutes to rinse the unbound Hg salt from the pores of the membrane and for safety reasons. The samples were then dried under atmospheric conditions for 1 h. and were sputter coated with gold before the analysis.

Table S1. Selected data[a] from the ICP-MS analyses[b] for the aqueous mother solution during the Hg^{2+} adsorption process by 10 mg of a polycrystalline sample of MOF **2** (center column) and the previously reported MOF **1**[25] (right column).

Time (min.)	$[Hg^{2+}]$	$[Hg^{2+}]$
0	9911	9863
1	5194	6764
5	1741	3454
10	978	1088
15	411	778
30	63.4	166
45	11.2	67.7
60	5.01	47.6
75	5.00	35.5
90	4.92	25.5
120	4.94	12.7
180	4.87	9.22
240	4.70	8.44
300	4.68	8.17
360	4.60	7.96
720	4.61	7.41
1440	4.60	7.43
4320	4.60	-

[a] Results are given as μg/L. [b] LOD: 0,012 μg/L

Table S2. Summary of Crystallographic Data for **2** and **$HgCl_2$@2**.[a]

Compound	**2**	**$HgCl_2$@2**
Formula	$C_{30}Cu_6CaH_{72}S_6N_6O_{37}$	$C_{30}Cl_2Cu_6CaH_{56}HgS_6N_6O_{29}$
M (g mol^{-1})	1722.61	1849.9701
λ (Å)	0.6889	0.6889
Crystal system	Hexagonal	Hexagonal
Space group	$P6_3$	$P6_3$
a (Å)	17.807	18.3828(13)
c (Å)	12.54520(10)	11.8283(10)
V (Å^3)	3445.20(3)	3461.6(6)
Z	2	2
ρ_{calc} (g cm^{-3})	1.661	1.775
μ (mm^{-1})	1.912	3.945
T (K)	100	100
θ range for data collection (°)	2.028 to 36.067	2.079 to 29.178
Completeness to θ = 25.0	100%	100%
Measured reflections	77003	50992
Unique reflections (Rint)	11411 (0.0632)	6584 (0.0676)
Observed reflections [$I > 2\sigma(I)$]	8560	5196
Goof	0.962	1.33
R^b [$I > 2\sigma(I)$] (all data)	0.0552(0.0676)	0.0770 (0.0920)
wR^c [$I > 2\sigma(I)$] (all data)	0.1824(0.1931)	0.2179(0.2281)

[a] Crystallographic Data for **1** can be found at ref.[58]

[b] $R = \sum(|F_o| - |F_c|)/\sum|F_o|$. [c] $wR = [\sum w(|F_o| - |F_c|)^2/\sum w|F_o|^2]^{1/2}$.

Table S3. Permeability data of distilled water and low mineral water through the tested membranes. The permeability values are calculated as the slope of the graph given by the measured flow (L m^{-2} h^{-1}) with respect to the pressure (bar).

Permeability of deionized water		**Permeability of Oligo-mineral water**	
Membrane	Permeability **(L m^{-2} h^{-1} bar^{-1})**	Membrane	Permeability **(L m^{-2} h^{-1} bar^{-1})**
1@Matrimid®	37.16	**1@Matrimid®**	35.72
2@Matrimid®	35.68	**2@Matrimid®**	35.84
Matrimid®	1.10	**Matrimid®**	1.08

Table S4. Residual Hg^{2+} concentration in the stock solution analyzed with the ICP-MS under static and dynamic adsorption processes for **1@Matrimid®, 2@Matrimid®** and neat **Matrimid®**, using deionized water with high concentrations of pollutant.

Mercury **concentration** in deionized water (µg/L)						
Static adsorption				**Dynamic adsorption**		
time (min)	Neat_Matrimid®	**1@Matrimid®**	**2@Matrimid®**	Number of cycles	**1@Matrimid®**	**2@Matrimid®**
0	2610	2610	2610	0	2210	2210
15	716	403	262	1	1234	1076
30	457	226	225	2	1137	1044
60	430	125	138	3	801	752
90	411	103	114	12	571	550
1440	369	98.0	87.1	36	420	390
2880	352	63.1	52.2	72	377	230
4320	348	52.8	47.5			

Table S5. Mineral water content concentration expressed in (mg L^{-1}).

Mineral water composition (mg L^{-1})	
Sodium	1.5
Bicarbonate	10
Fluoride	< 0.10
Calcium	2.9
Nitrate	0.81

Table S6. Selected data from the ICP-MS analyses for the Hg^{2+} as static and dynamic adsorption for **1@Matrimid®, 2@Matrimid®** and pure **Matrimid®** in oligo mineral water with added high concentrations of pollutant.

Mercury concentration in oligo mineral water I (µg/L)						
Static adsorption				**Dynamic adsorption**		
time (min)	Neat_Matrimid®	**1@Matrimid®**	**2@Matrimid®**	Number of cycles	**1@Matrimid®**	**2@Matrimid®**
0	2220	2220	2220	0	2090	2090
15	1170	740	520	1	1220	890
30	950	580	228	2	1040	860
60	900	490	120	3	885	645
90	830	405	60.2	12	531	398
1440	662	355	55.9	36	427	310
2880	538	210	50.8	72	380	238
4320	500	160	40.9			

Table S7. Selected data from the ICP-MS analyses for the Hg^{2+} as static and dynamic adsorption for **1@Matrimid®, 2@Matrimid®** and pure **Matrimid®** in oligo-mineral water with added low concentrations of pollutant.

Mercury concentration in oligo mineral water II (µg/L)						
Static adsorption				**Dynamic adsorption**		
time (min)	Neat_Matrimid®	**1@Matrimid®**	**2@Matrimid®**	Number of cycles	**1@Matrimid®**	**2@Matrimid®**
0	373	373	373	0	330	330
15	227	227	228	1	236	131
30	219	206	195	2	190	81.5
60	200	170	129	3	133	64.6
90	144	98.9	55.3	12	13.1	6.22
1440	97.8	52.8	32.5	36	2.33	1.89
2880	88.1	21.4	10.1	72	1.78	1.26
4320	76.6	1.85	< LOD[a]			

[a] LOD = 0.1 $\mu g L^{-1}$

Table S8. Hg^{2+} removal (%) of **1@Matrimid®, 2@Matrimid®** and pure **Matrimid®** for static and dynamic adsorption.

Static adsorption									
time (min)	Hg^{2+} solution in **Deionized water**			Hg^{2+} solution in **Oligo mineral water I**			Hg^{2+} solution in **Oligo mineral water II**		
	Neat_Matrimid®	**1**	**2**	Neat_Matrimid®	**1**	**2**	Neat_Matrimid®	**1**	**2**
0	0	0	0	0	0	0	0	0	0
15	72.6	84.6	90.0	47.3	66.7	76.6	39.0	39.1	38.7
30	82.5	91.3	91.8	57.2	73.9	89.7	41.3	44.7	47.6
60	83.5	95.2	94.7	59.,5	77.9	94.6	46.4	54.5	65.3
90	84.3	96.1	95.6	62.6	81.8	97.3	61.3	73.5	85.2
1440	85.7	96.2	96.7	70.2	84.0	97.5	73.8	85.8	91.3
2880	86.5	97.6	98.0	75.8	90.5	97.7	76.4	94.3	97.3
4320	86.7	98.0	98.2	77.5	92.8	98.2	79.5	99.5	<LOD

Dynamic adsorption							
time (min)	Number of cycles	Hg^{2+} solution in **Deionized water**		Hg^{2+} solution in **Oligo mineral water I**		Hg^{2+} solution in **Oligo mineral water II**	
		1	**2**	**1**	**2**	**1**	**2**
0	0	0	0	0	0	0	0
40	1	44.1	51.2	41.6	57.4	28.6	60.3
80	2	48.5	52.7	50.2	58.9	42.4	75.3
120	3	63.7	65.9	57,7	69.1	59.7	80.4
8 hours	12	74.1	75.1	74.6	81.0	96.0	98.1
24 hours	36	81.0	82.3	79.6	85.2	99.3	99.4
48 hours	72	82.9	89.6	81.8	88.6	99.5	99.6

Table S9. Adsorption expressed as µg/cm^2 for **1@Matrimid®, 2@Matrimid®** and pure Matrimid® in static and dynamic adsorption, obtained for the reported experiments (100 mL of polluted solutions) calculated as following:

$$^{a}(C_i\text{-}C_f)/\text{ surface area}^{b}\ cm^2$$

Static adsorption (µg/cm^2)			
membrane	$^{b}Hg^{2+}$ solution in **Deionized water**	Hg^{2+} solution in **Oligo mineral water I**	Hg^{2+} solution in **Oligo mineral water II**
Neat_Matrimid®	130.4	99.2	17.1
1@ Matrimid®	147.5	118.8	26.8
2@ Matrimid®	147.8	125.7	26.9
Dynamic adsorption (µg/cm^2)			
Membrane	Hg^{2+} solution in **Deionized water**	Hg^{2+} solution in **Oligo mineral water I**	Hg^{2+} solution in **Oligo mineral water II**
1@ Matrimid®	137.9	123.6	23.7
2@ Matrimid®	143.0	133.8	23.7

The green section underlines the reached potable water limits.

[a] Concentrations expressed in ppb (from Tables S4, S6-S7).

[b] In the static adsorption, the membrane's area measured 17.34 cm^2 whereas in the dynamic the exposed area was of 13.84 cm^2.

Table S10. Hg^{2+} removal (μg L^{-1}) of **1@Matrimid®, 2@Matrimid®** and pure **Matrimid®** after three regeneration cycles for static and dynamic adsorption of Hg^{2+} in oligo mineral water. Values indicate the residual concentration in the solutions.

Static adsorption				Dynamic adsorption		
Time (min)	**Matrimid®**	**1@Matrimid®**	**2@Matrimid®**	Number of cycle	**1@Matrimid®**	**2@Matrimid®**
0	361	361	361	0	300	300
15	269	231	230	1	248	234
30	240	229	182	2	188	176
60	187	155	135	3	141	84.3
90	151	105	102	12	135	61.7
1440	111	77.2	69.5	36	82.4	54.0
2880	95.8	45.4	43.1	72	40.7	35.9
4320	66.6	37.0	29.7			

Table S11. Hg^{2+} removal (%) of **1@Matrimid®, 2@Matrimid®** and pure **Matrimid®** after three regeneration cycles for static and dynamic adsorption of Hg^{2+} in oligomineral water.

Static adsorption				*Dynamic adsorption*		
Time (min)	**Matrimid®**	**1@Matrimid®**	**2@Matrimid®**	Cycle	**1@Matrimid®**	**2@Matrimid®**
15	28.0	38.1	38.2	1	24.7	29.0
30	35.7	38.7	51.1	2	43.1	46.6
60	49.8	58.3	63.7	3	57.2	74.5
90	59.5	71.9	72.7	12	59.1	81.3
1440	70.3	79.3	81.4	36	75.0	83.6
2880	74.3	87.8	88.4	72	87.7	89.1
4320	82.1	90.1	92.0			

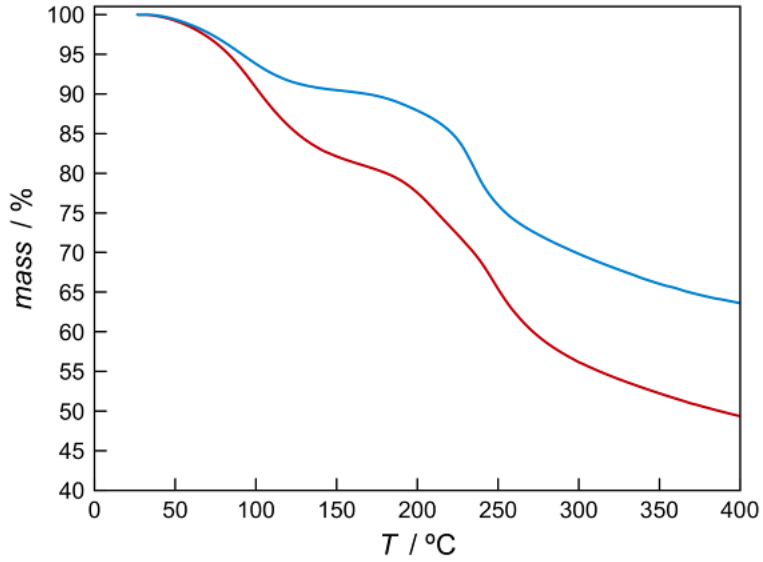

Figure S1. Thermo-Gravimetric Analysis (TGA) of **2** (red) and **$HgCl_2$@2** (blue) under dry N_2 atmosphere.

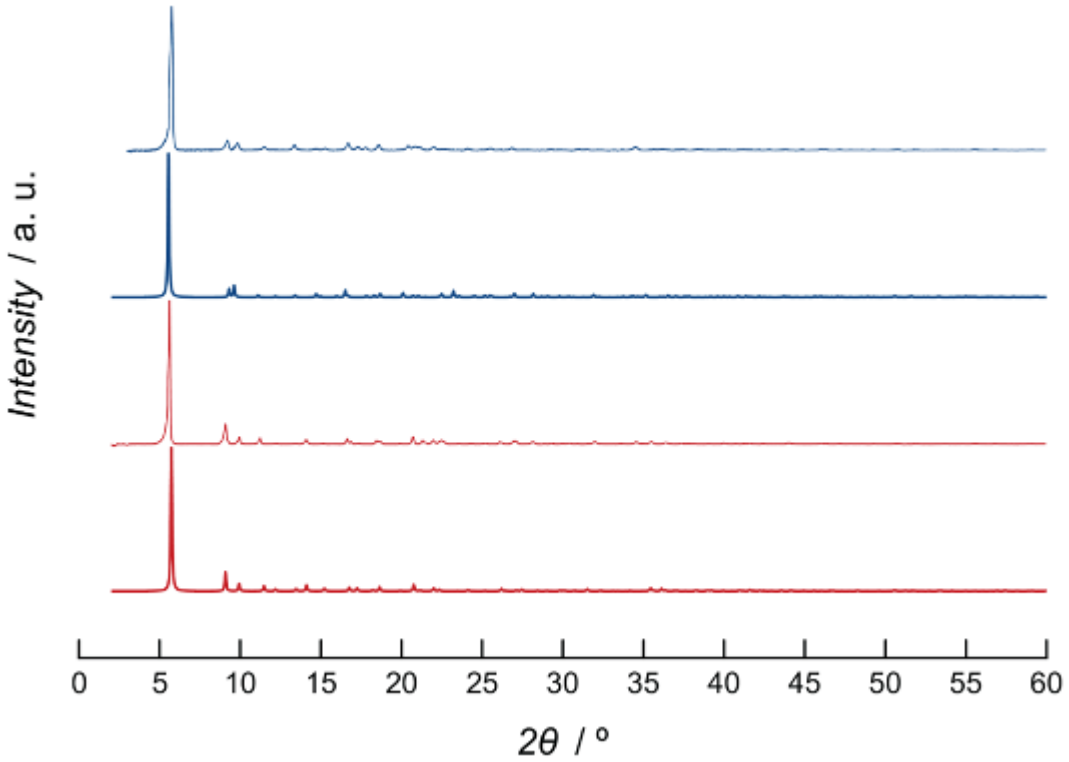

Figure S2. a) Calculated (bold lines) and experimental (solid lines) PXRD pattern profiles of **2** (red) and **$HgCl_2$@2** (blue) in the 2θ range 2.0–60.0°.

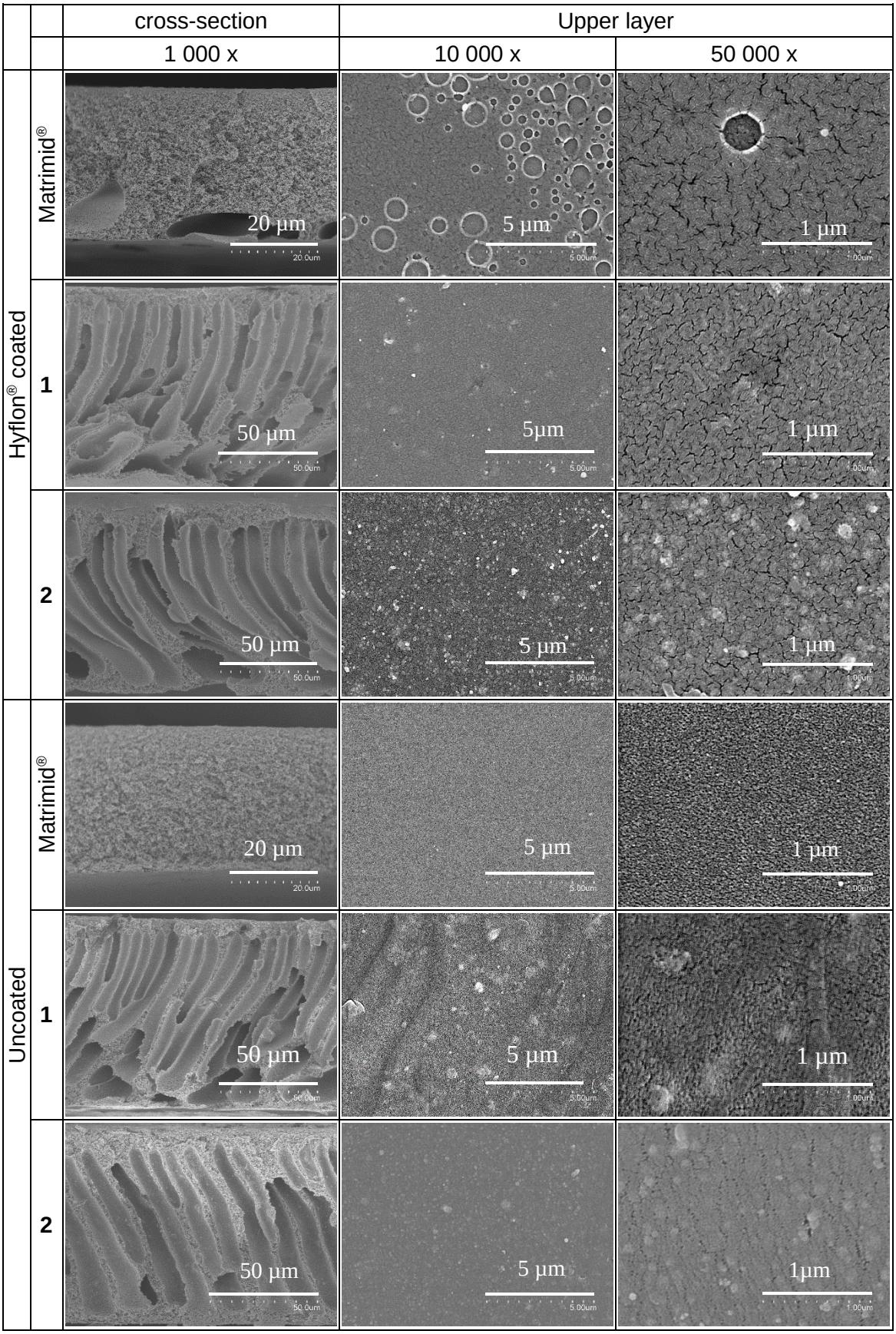

Figure S3. SEM images of mixed matrix membranes **1@Matrimid®** and **2@Matrimid®** and of the neat Matrimid® membrane at magnification of 1000 X, 10.000 X and 50. 000 X at an accelerating voltage of 10 Kv. The Hyflon® coated and uncoated membranes are compared.

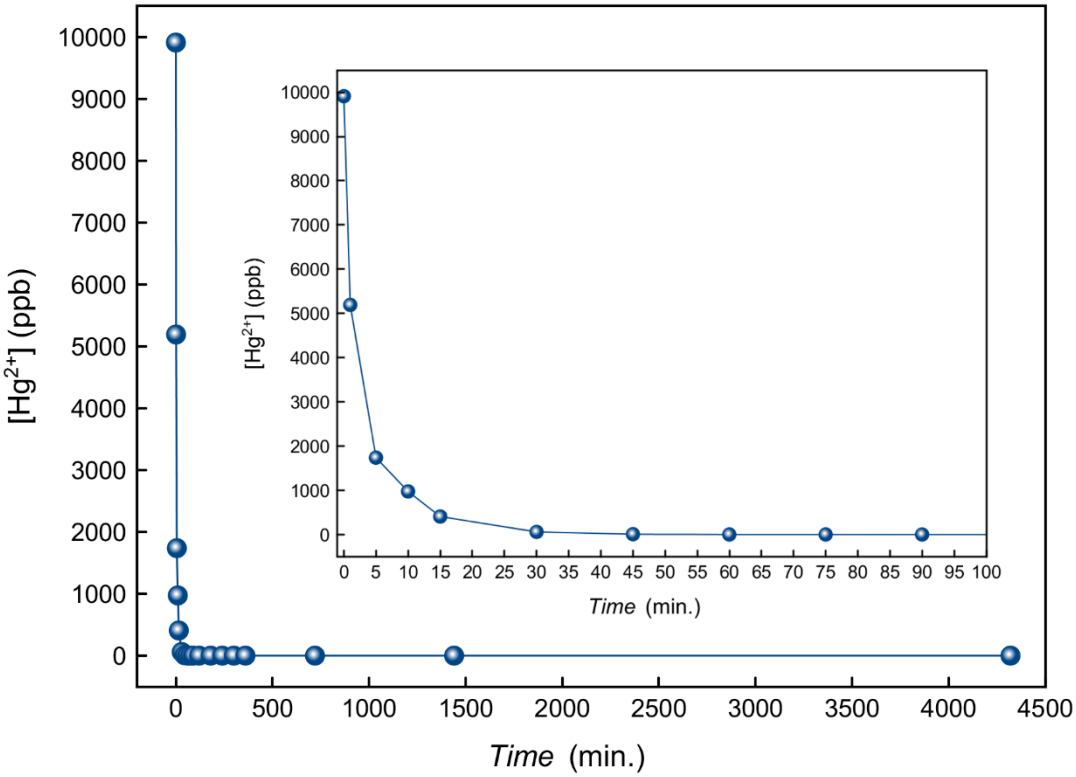

Figure S4. Kinetic profile of the mercury(II) capture by MOF **2** measured as the decrease of the metal concentration with time after soaking 10 mg of a polycrystalline sample in an aqueous solution containing 10 ppm of $HgCl_2$ in the 0-72 h. interval (ICP-MS data collected in Table S1). The inset shows the capture in the time interval of 0-100 min.

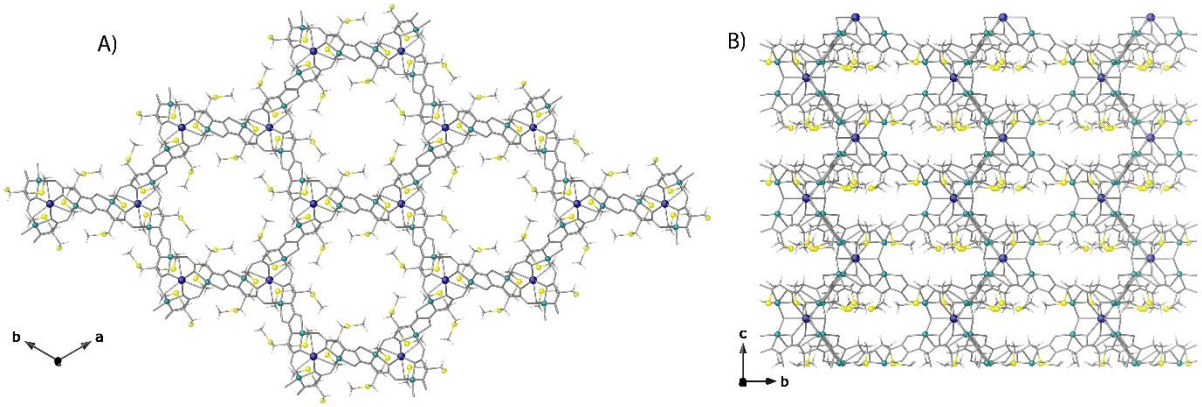

Figure S5. X-ray crystal structure of **2**: A) View along *c* and B) *a* crystallographic axis. Atom color code: All atoms from the coordination network are represented as grey sticks, with the only exception of copper(II) (cyan spheres), calcium(II) (blue spheres) and sulfur atoms (yellow spheres) from methylcysteine residues residing in pores and conveying receptor properties to the MOF towards Hg^{2+} metal ions.

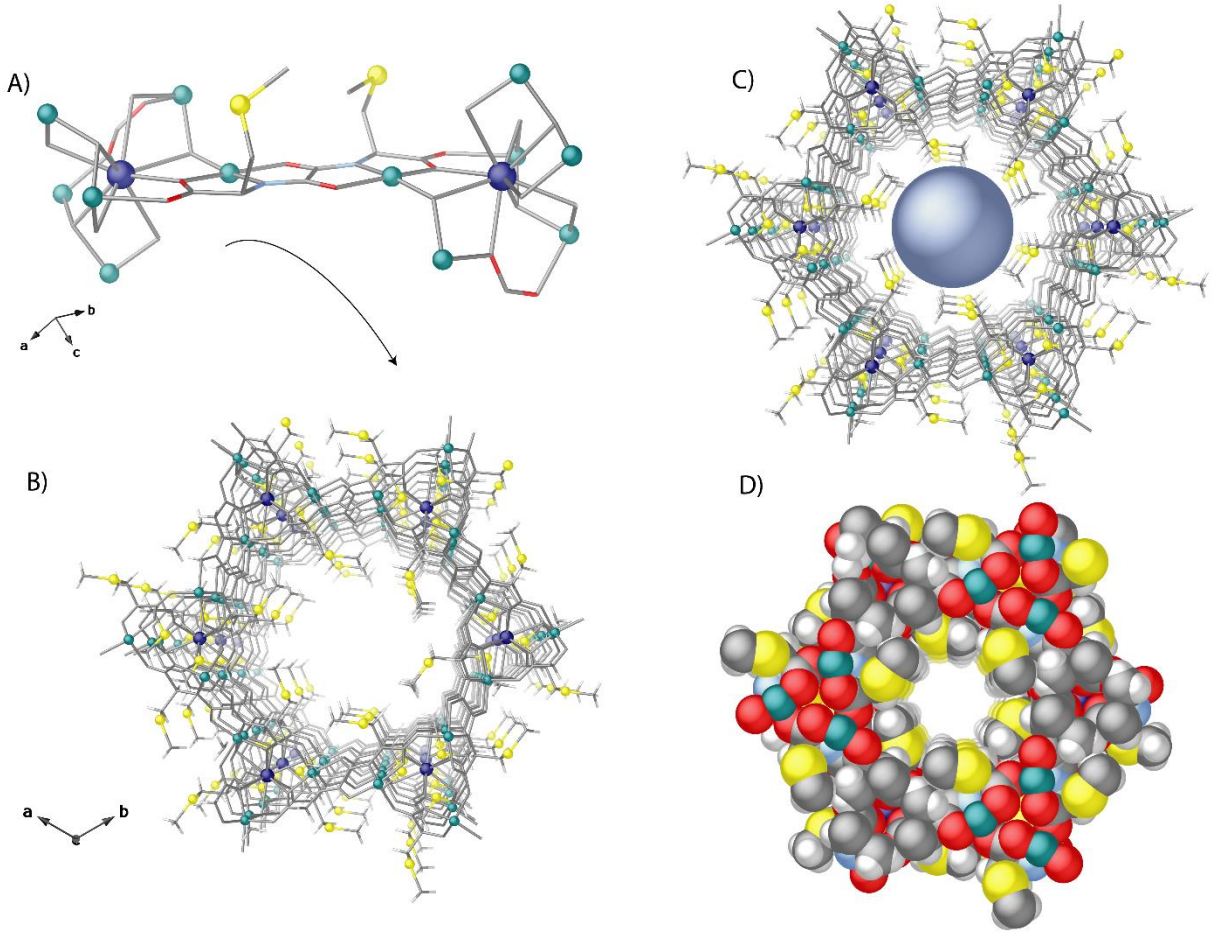

Figure S6. Details on X-ray crystal structure of **2**: A) Dicopper(II) units, {Cu^{II}_2[(S,S)-Mecysmox]} acting as linkers between the Ca^{II} ions through the carboxylate groups and perspective views of a single channel along *c* crystallographic axis B) underlining the large voids through the representation of a dummy atom (blue sphere in pore) C); representation of a single channel with space filling model (with Van der Waals radii) D). Atom color code: All atoms from the coordination network are represented as grey sticks, with the only exception of copper(II) (cyan spheres), calcium(II) (blue spheres) and sulfur atoms (yellow spheres) from methylcysteine residues residing in pores. In A and D carbon, nitrogen and oxygen atoms have been depicted in grey, light blue and red color.

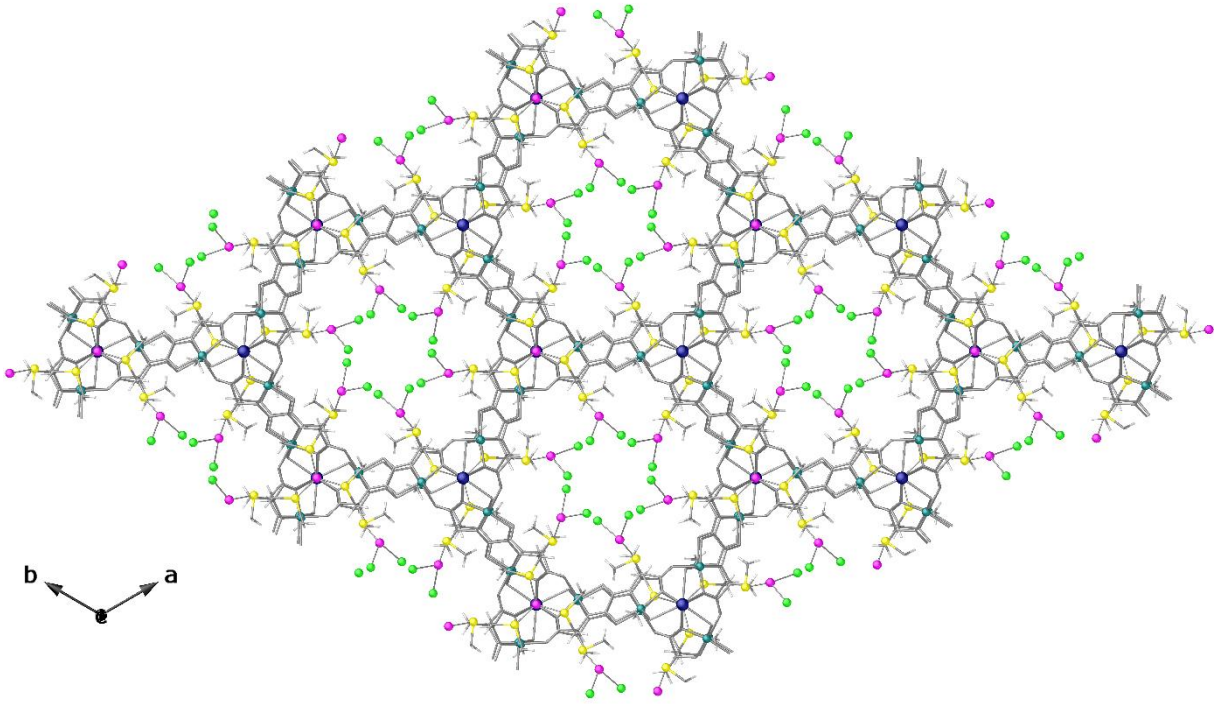

Figure S7. X-ray crystal structure of **$HgCl_2$@2** with $HgCl_2$ molecules linked by S atoms of methylcysteine residues, densely packed within channel**s**. Atom colour code: All atoms from the coordination network are represented as grey sticks, with the only exception of copper(II) (cyan spheres), calcium(II) (blue spheres) and sulfur atoms (yellow spheres) from methylcysteine residues residing in pores together with Hg(II) and chloride represented by purple and green spheres, respectively.

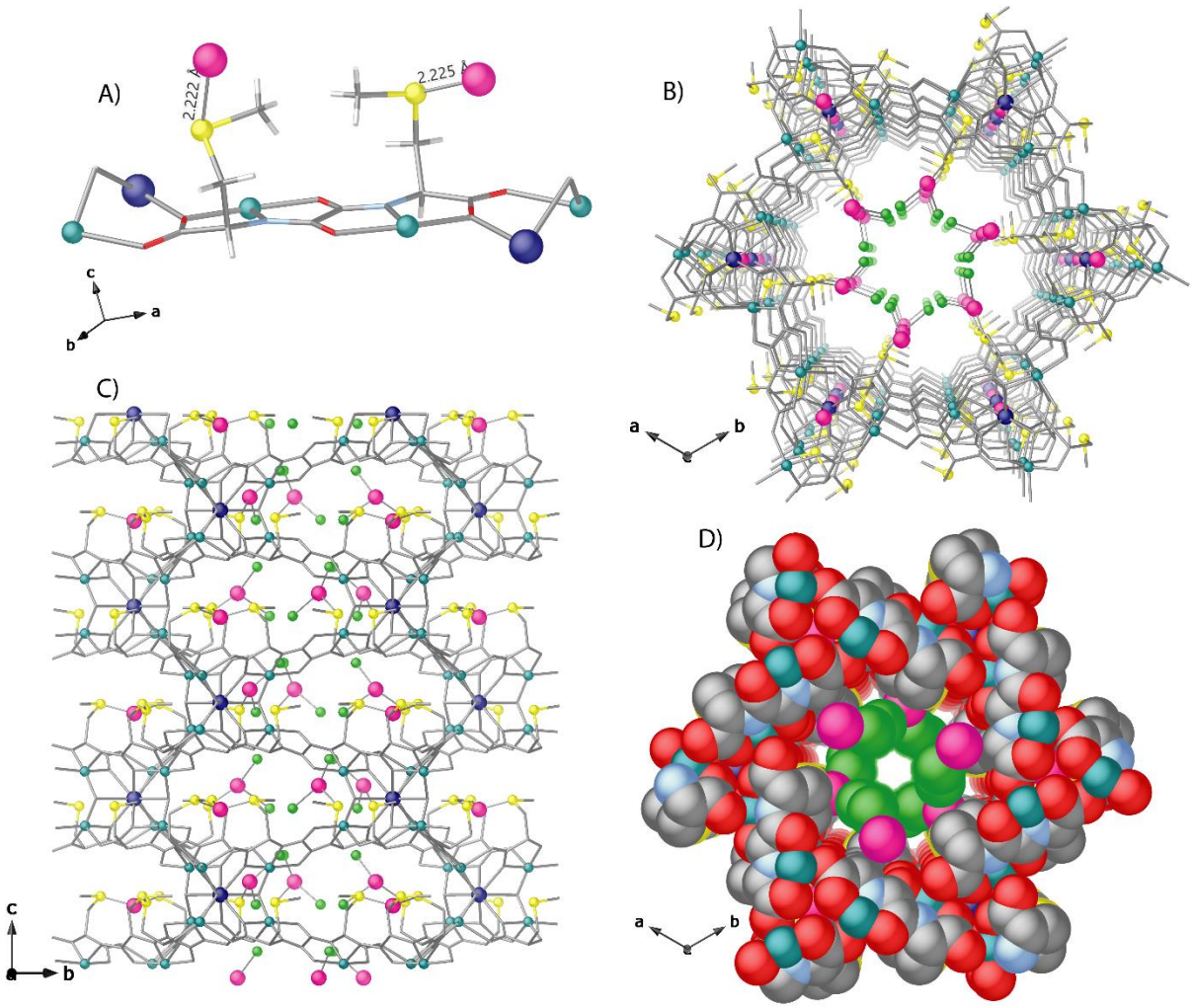

Figure S8. Details of crystal structure of **$HgCl_2$@2**: A) Dicopper(II) units, {Cu^{II}_2[(S,S)-Mecysmox]} acting as linkers *via* methylcysteine *arms* towards $HgCl_2$ molecules B) perspective view of a single channel of **$HgCl_2$@2** crystal structure along *c* (B) and *a* crystallographic axis (C) where the large voids are filled by 'captured' pollutant molecules; D) representation of a single channel with space filling model (with Van der Waals radii. Atom color code: All atoms from the coordination network are represented as grey sticks, with the only exception of copper(II) (cyan spheres), calcium(II) (blue spheres) and mercury(II) (purple spheres), Chloride (green spheres) and sulfur atoms (yellow spheres) from methylcysteine residues residing in pores. In A and D carbon, nitrogen and oxygen atoms have been depicted in grey, light blue and red color.

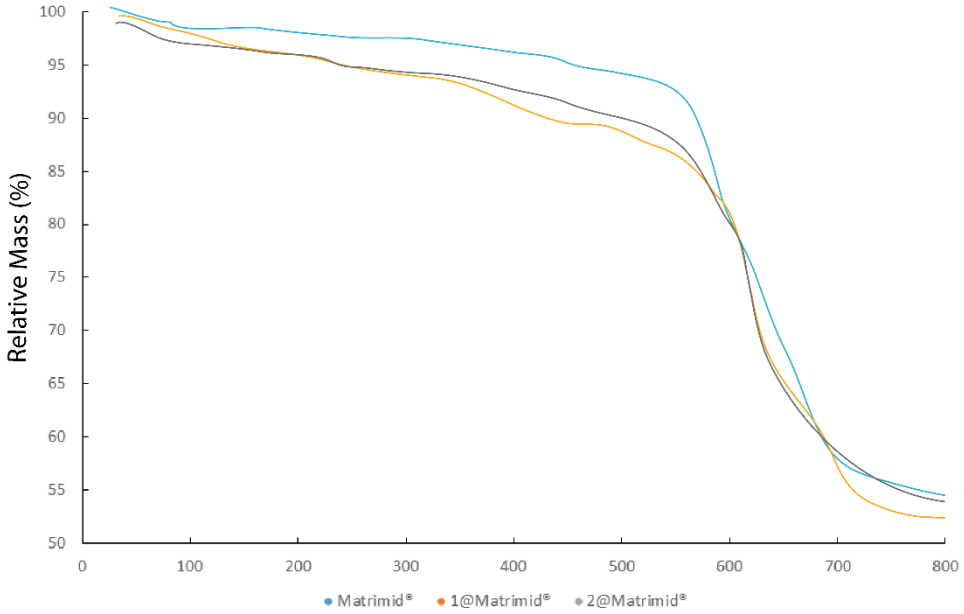

Figure S9. Thermo Gravimetric Analysis TGA of the **1@Matrimid®**, **2@Matrimid®** and a pure **Matrimid®** shown for comparison.

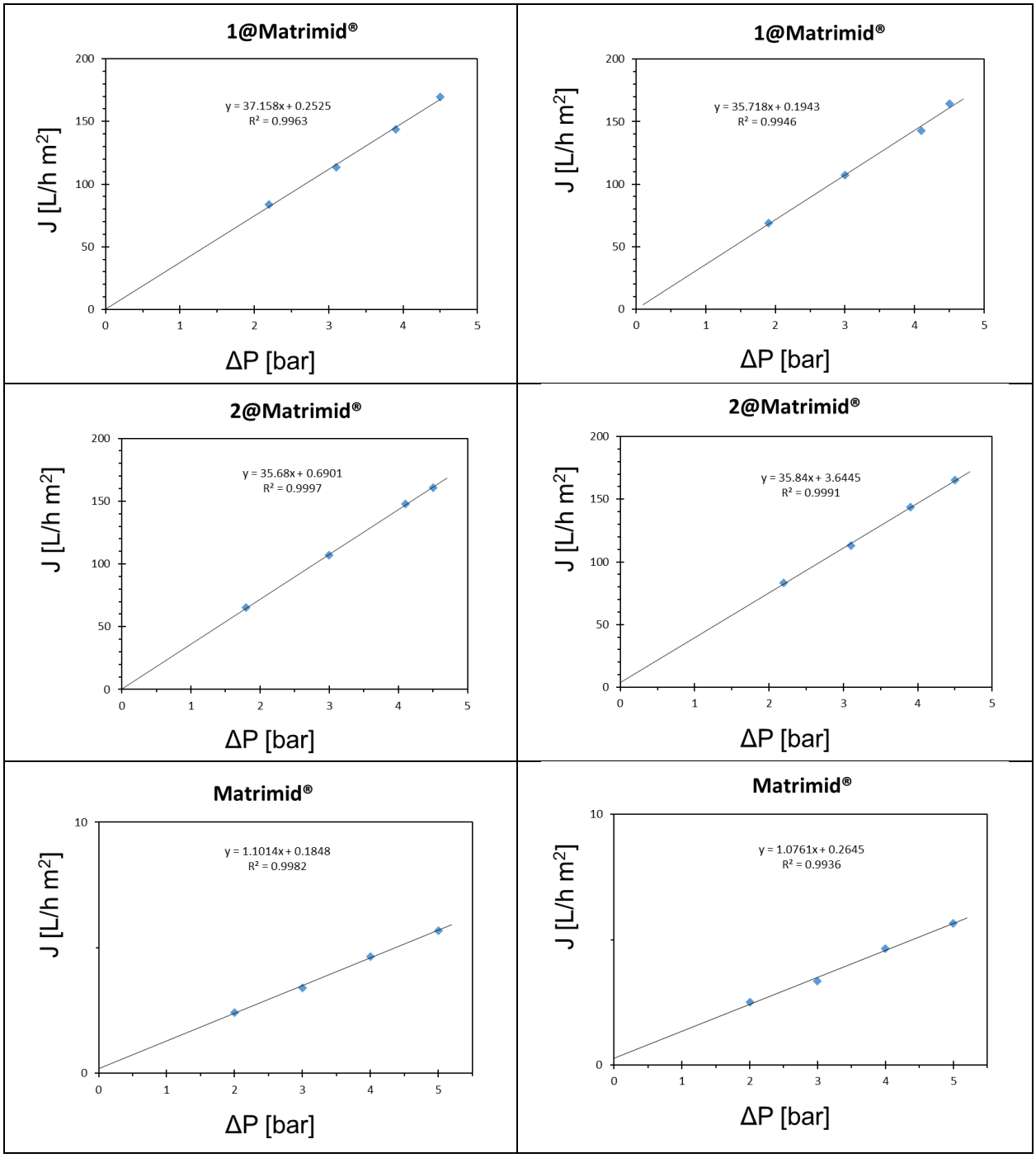

Figure S10. Water flux (J) with distilled water and low mineral water through the tested membranes as a function of the applied pressure. The permeability is calculated from the slope of the curves and the values are reported in Table S3.

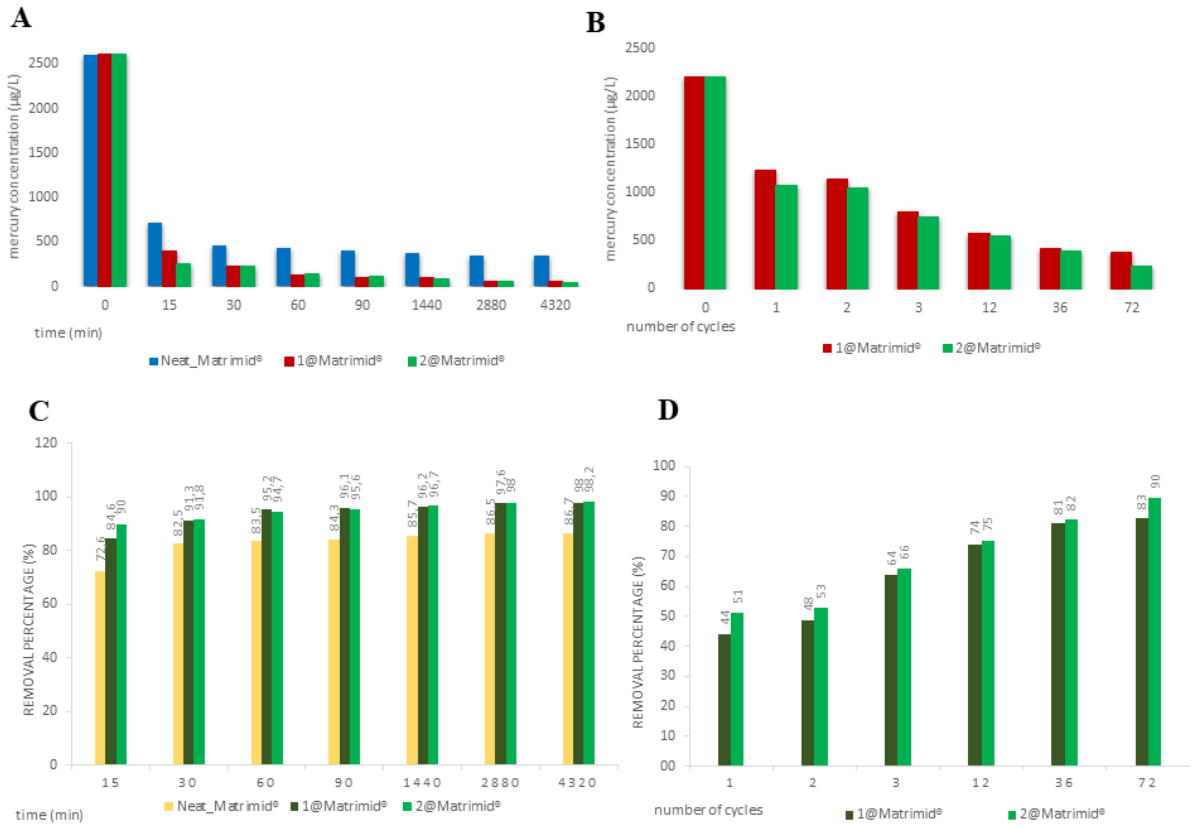

Figure S11. Kinetic profiles of the mercury(II) capture by **1@Matrimid®**, **2@Matrimid®** and a pure Matrimid® membrane after soaking a circular flat membrane (surface of 17.34 cm^2) in an aqueous solution of $HgCl_2$ in the 0-72 h interval. The initial [Hg^{2+}] in deionized water are 2.60 ppm and 2.21 ppm for static (A) and dynamic (B) adsorption, respectively (Table S4). (B) Removal efficiencies (%) of **1@Matrimid®**, **2@Matrimid®** and a pure Matrimid® membrane under the same conditions for static (C) and dynamic (D) adsorption (Table S8). 48 h corresponds to 72 cycles of microfiltration (the duration of a cycle for the recirculation of 100 mL of solution is 40 minutes).

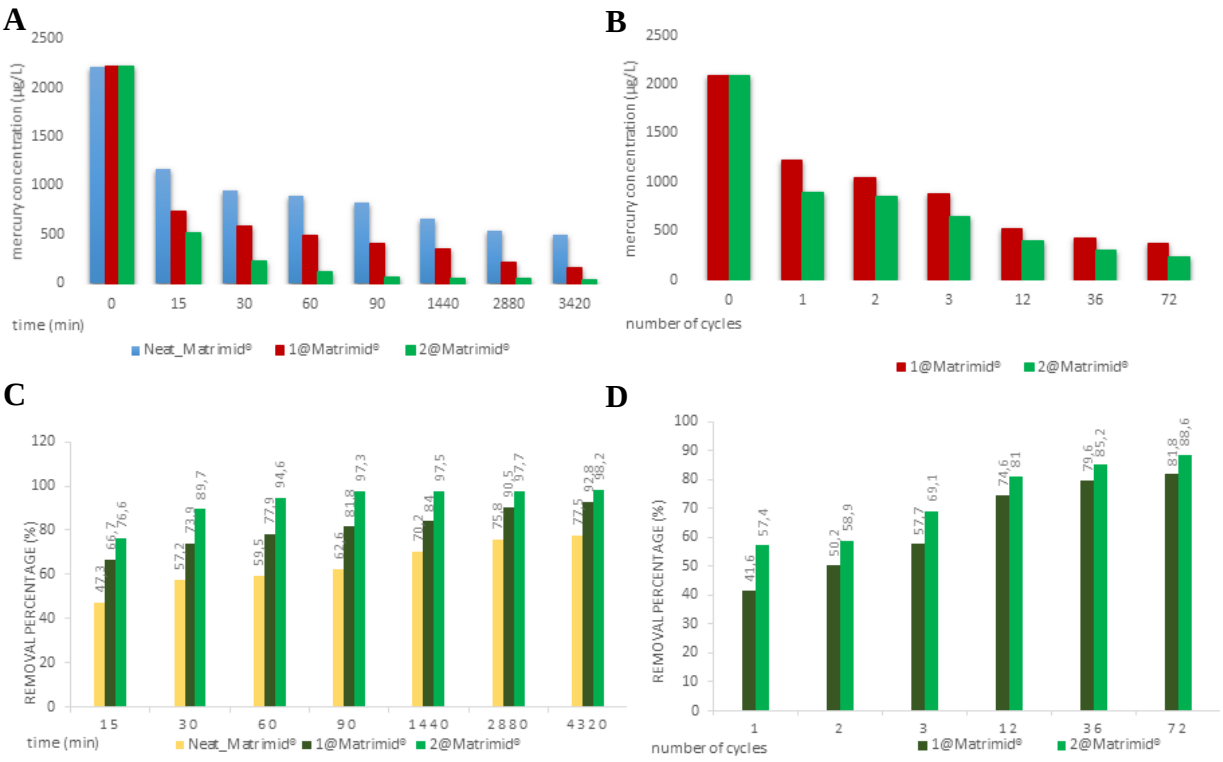

Figure S12. Kinetic profiles of the mercury(II) capture by **1@Matrimid®**, **2@Matrimid®** and a pure Matrimid® membrane after soaking a circular flat membrane (surface of 17.34 cm^2) in an aqueous solution of $HgCl_2$ in the 0-72 h interval. The initial [Hg^{2+}] in oligo mineral water are 2.22 ppm and 2.09 ppm for static (A) and dynamic (B) adsorption, respectively (Table S6). (B) Removal efficiencies (%) of **1@Matrimid®**, **2@Matrimid®** and a pure Matrimid® membrane under the same conditions for static (C) and dynamic (D) adsorption (Table S8). 48 h corresponds to 72 cycles of microfiltration (the duration of a cycle for the recirculation of 100 mL of solution is 40 minutes).

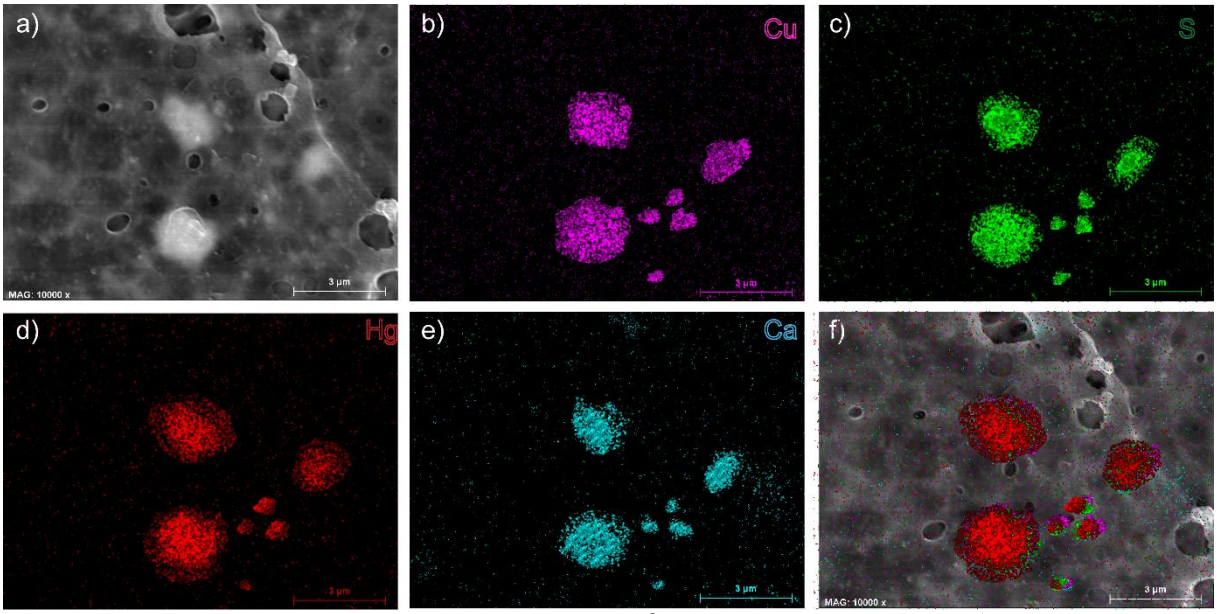

Figure S13. (a) Backscattered SEM image of **1@Matrimid®** and the corresponding EDX elemental mapping for Cu (b), S (c), Hg (d) and Ca (e) elements. (f) Superposition of images a-e. The backscattering detector highlights the MOF particles as brighter areas due to crystalline MOF structure and to the presence of heavier atoms in the MOF than in the polymer matrix.

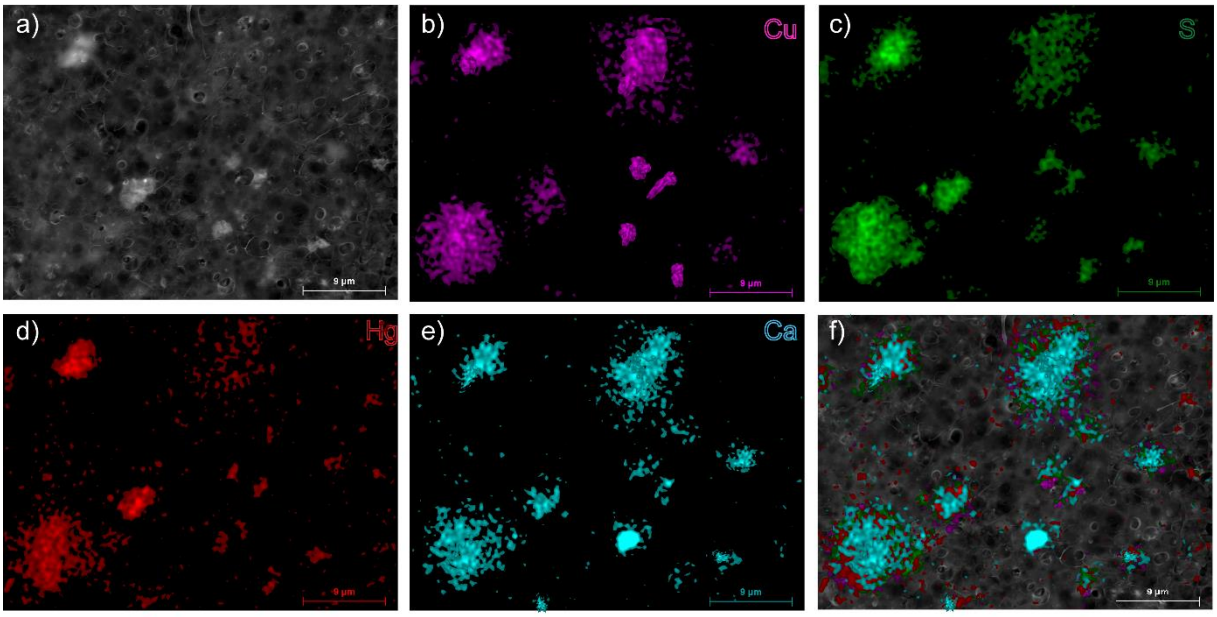

Figure S14. (a) Backscattered SEM image of **2@Matrimid®** and the corresponding EDX elemental mapping for Cu (b), S (c), Hg (d) and Ca (e) elements. (f) Superposition of images a-e. The backscattering detector highlights the MOF particles as brighter areas due to crystalline MOF structure and to the presence of heavier atoms in the MOF than in the polymer matrix.

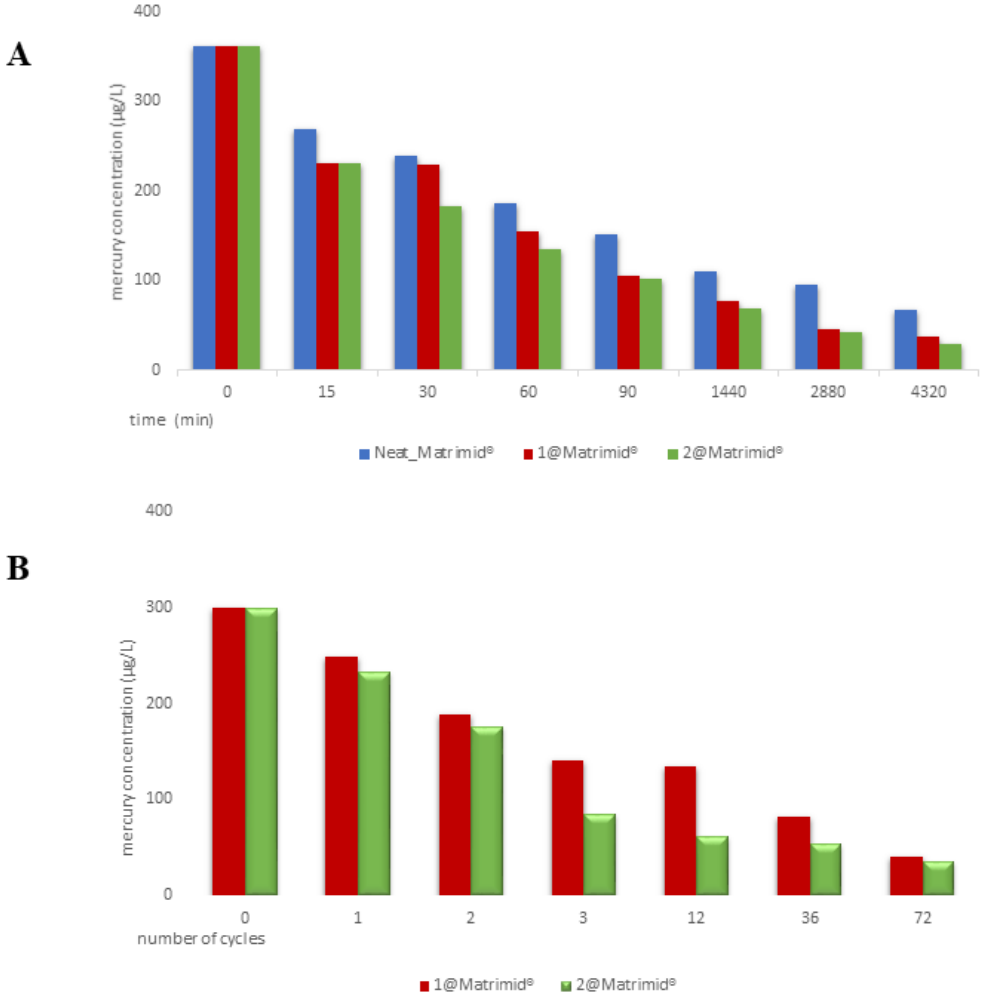

Figure S15. Adsorption performance (µg L^{-1}) of **1@Matrimid®**, **2@Matrimid®** membranes reused after three regeneration cycles for static (A) and dynamic (B) adsorption of Hg^{2+} (data from Table S10).

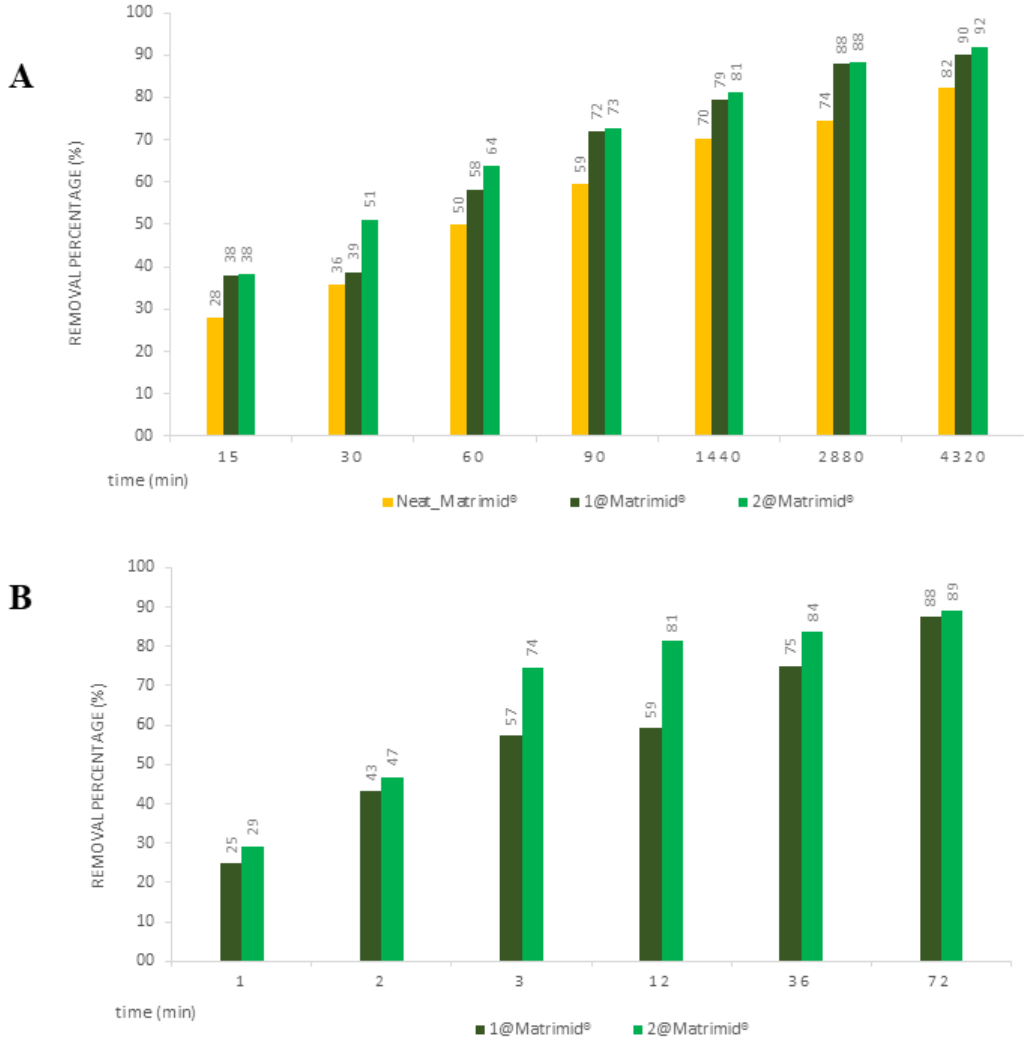

Figure S16. Adsorption performance (%) of **1@Matrimid®**, **2@Matrimid®** membranes reused after three regeneration cycles for static (A) and dynamic (B) adsorption of Hg^{2+} (data from Table S11).